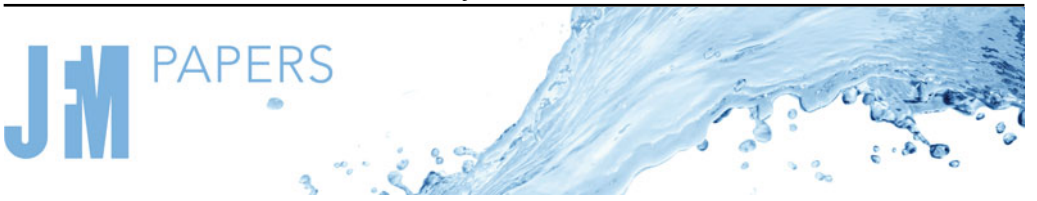
J. Fluid Mech. (2025), *vol.* 1021, A51, doi:10.1017/jfm.2025.10758



Reconfiguration and hydrodynamic forces on flexible vegetation under orthogonal wave–current conditions

Zichen Xu[1] **and Jiarui Lei**[1]

[1]Department of Civil and Environmental Engineering, National University of Singapore, 21 Lower Kent Ridge Road, Singapore 119077, Republic of Singapore

Corresponding author: Jiarui Lei, jlei@nus.edu.sg

(Received 7 March 2025; revised 20 September 2025; accepted 21 September 2025)

The reconfiguration of flexible aquatic vegetation and the associated forces have been extensively studied under two-dimensional flow conditions – such as unidirectional currents, pure waves and co-directional wave–current flows. However, behaviour under more complex, orthogonal wave–current flows remains largely unexplored. In coastal environments, such orthogonal flows arise when waves propagate perpendicular to a longshore current. To improve understanding of how aquatic vegetation helps protect coastlines and attenuates waves, we extended existing effective-length scaling laws that were validated in pure currents, pure waves, and co-directional waves and currents to orthogonal wave–current conditions by introducing new definitions of the Cauchy number. Experiments were conducted in a wave–current basin, where cylindrical rubber stems were mounted on force transducers to measure hydrodynamic forces. Stem velocities were extracted from video recordings to compute the relative velocity between the flow and the stems. Incorporating the phase shift between flow and stem velocities into the force models significantly improved predictions. Comparison of predicted and measured forces showed good agreement for both pure wave and wave–current scenarios, underscoring the importance of phase shifts and velocity reduction for force estimation. Our hypothesised effective-length scaling parameters under wave–current conditions were validated, but with a higher scaling coefficient due to inertial effects from the larger material aspect ratio. These findings offer new insights into the hydrodynamics of flexible structures under complex coastal flow conditions.

Key words: coastal engineering, hydraulics, wave-structure interactions

© The Author(s), 2025. Published by Cambridge University Press. This is an Open Access article, distributed under the terms of the Creative Commons Attribution licence (https://creativecommons.org/licenses/by/4.0/), which permits unrestricted re-use, distribution and reproduction, provided the original article is properly cited.

https://doi.org/10.1017/jfm.2025.10758 Published online by Cambridge University Press

1. Introduction

Aquatic vegetation provides essential ecosystem services (Barbier *et al.* 2011). It enhances biodiversity by providing habitat and shelter for fisheries (Costanza *et al.* 1997), and by supplying food for larger herbivorous animals such as dugongs and green turtles (Waycott, Longstaff & Mellors 2005). Shoreline vegetation attenuates incoming waves, mitigating coastal erosion caused by wave impact (Koch *et al.* 2009; Barbier *et al.* 2011). Furthermore, submerged macrophytes contribute to nutrient retention in local ecosystems (Barko & James 1998) and act as carbon sinks, sequestering more carbon per hectare annually than tropical rainforests (Fourqurean *et al.* 2012). Given the critical role of aquatic vegetation in these processes, its protection and restoration have become a central focus in coastal management (Greiner *et al.* 2013). Understanding vegetation dynamics across various flow conditions is essential for predicting its coastal protection benefits, as well as its role in particle retention and carbon sequestration.

Numerous studies have examined wave attenuation by vegetation, using both laboratory experiments with model vegetation (Mendez & Losada 2004; Augustin, Irish & Lynett 2009; Stratigaki *et al.* 2011; Xu & Lei 2024*b*), real vegetation (Maza, Lara & Losada 2016; van Wesenbeeck *et al.* 2022; Xie & Lei 2025) and field observations (Bradley & Houser 2009; Paul & Amos 2011; Infantes *et al.* 2012). Some of these investigations have specifically investigated the role of vegetation flexibility in wave damping. For instance, Mullarney & Henderson (2010) formulated an analytical model based on cantilever beam theory to simulate the motion of single-stemmed vegetation, such as sedges. Their findings indicated that wave dissipation by flexible vegetation was only 30 % of that observed for rigid vegetation. Similarly, Houser, Trimble & Morales (2015) explored how blade flexibility influences the drag coefficient and, consistent with Mullarney & Henderson (2010), found that increased flexibility led to a reduction in drag force.

Although waves and currents often coexist in coastal environments, relatively few studies have investigated how their combined effects influence the hydrodynamic response of flexible vegetation and its wave-damping capacity. Losada, Maza & Lara (2016) conducted laboratory experiments with real vegetation and observed that wave attenuation increased when the current opposed wave propagation, but decreased when the current aligned with it. They proposed a wave energy dissipation model incorporating vegetation deflection by replacing the full blade length, l, with the deflected height, l_d, which represents the vertical distance from the bed to the time-averaged blade tip position.

Another approach to characterising vegetation–flow interaction involves the concept of effective blade length, which quantifies the impact of reconfiguration on drag forces experienced by an individual blade in co-directional waves and currents. Originally introduced by Alben, Shelley & Zhang (2002), this concept has been developed and validated for various flow regimes, including pure currents (Luhar & Nepf 2011, 2013; Lei & Nepf 2021), pure regular waves (Luhar, Infantes & Nepf 2017; Lei & Nepf 2019*b*), pure internal solitary waves (Sun, You & Lei 2024), and co-directional waves and currents (Lei & Nepf 2019*a*; Schaefer & Nepf 2024). The effective length l_e represents the equivalent length of a rigid blade that experiences the same drag as a flexible blade of actual length l. Typically, reconfiguration reduces drag force, resulting in $l_e < l$. This drag reduction occurs due to a decrease in the plant's frontal area, streamlining of the blade, and, in wave environments, blade motion that lowers the relative velocity between the blade and the surrounding water.

Despite these advances, a comprehensive predictor for vegetation dynamics under orthogonal wave–current conditions, where the current is perpendicular to wave propagation, remains lacking. Our study addresses this knowledge gap by investigating the response of flexible vegetation under orthogonal wave–current conditions through

https://doi.org/10.1017/jfm.2025.10758 Published online by Cambridge University Press

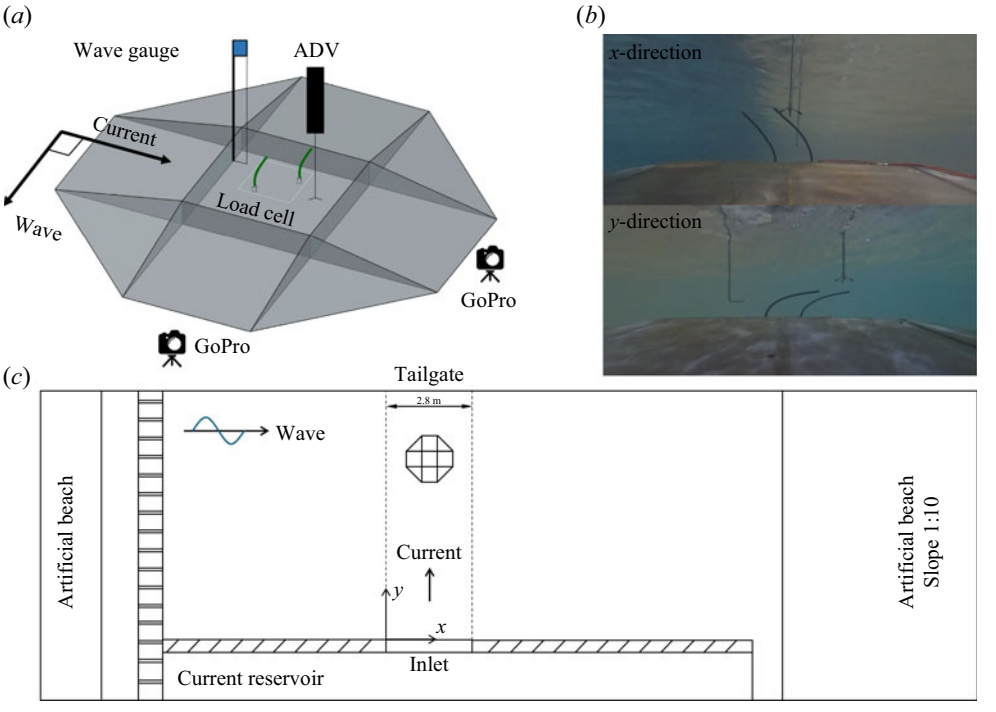


Figure 1. (*a*) Schematics of the truncated pyramid and instrument installation. (*b*) Sample GoPro frames showing stem motion in the x- and y-directions. (*c*) Illustration of the wave–current basin and the position of the truncated pyramid.

controlled laboratory experiments. Specifically, we quantify how vegetation motion and drag forces are modified by wave–current interactions. By integrating force measurements, velocity analysis and video-based motion tracking with the Morison equation, we establish a framework for predicting hydrodynamic forces on flexible vegetation under orthogonal wave–current conditions. Finally, we evaluate whether scaling laws developed for pure currents, pure waves, and co-directional waves and currents can be adapted to the more complex orthogonal case.

2. Methods and data processing

2.1. *Experimental set-up and flow conditions*

The experimental tests were conducted in the wave–current basin at the Hydraulic Engineering Laboratory of the National University of Singapore. This basin, measuring 33 m in length, 10 m in width and 0.9 m in depth, is uniquely designed to generate orthogonal waves and currents. A 19 m $\times$ 1.5 m section was partitioned to create a reservoir that facilitates current recirculation. The current enters the main basin through a single opening with width of 2.8 m at a 90° angle to the waves and exits through an adjustable weir. Two 75 HP centrifugal pumps recirculate the flow from the basement tank to the roof tank (Lim & Madsen 2016). The current speed is controlled by adjusting the valve opening, weir height and water level in the roof tank. The wave propagation direction is defined as the x-direction, while the current flows along the y-direction (figure 1).

Waves were generated using a piston-type wave maker with 13 independently controlled paddles, each driven by an electric servo motor. A 1 : 10 sloped artificial gravel beach was

https://doi.org/10.1017/jfm.2025.10758 Published online by Cambridge University Press

installed to minimise wave reflection. Following the method of Goda & Suzuki (1976), wave reflection was measured using two wave gauges, yielding a reflection coefficient of 10 %. This study focused exclusively on regular waves, with a constant water depth of $h = 0.3$ m measured from the top of a false bottom. The experiments covered five wave periods ($T = 1.0$, 1.2, 1.4, 1.6, 2.0 s) and four wave amplitudes ($a_w = 0.03$, 0.04, 0.05, 0.06 m) (see the detailed test cases and results in Appendix A). Orthogonal wave–current flows were classified into two categories: wave–current flows with high current speed (WCHC) and wave–current flows with low current speed (WCLC), corresponding to current speeds of $u_c = 0.16$ m s^{-1} and $u_c = 0.06$ m s^{-1}, respectively. The flow conditions in this study closely resemble those observed in natural coastal environments.

To mimic individual elements of flexible vegetation, cylindrical rods were selected due to their uniform second moment of inertia, which suppresses torsional motion. As a result, torsion effects on vegetation rods were not considered in this study. Furthermore, in this study, the second moment of inertia is given as $I = \pi d^4/64$. Two EPDM-based materials with differing flexibilities were tested, denoted HF (high flexibility) and LF (low flexibility). The Young's modulus (E) of each material was measured using a low-force tensile strength tester (Instron 5969). The material LF ($E = 5.36$ MPa, $\rho_v = 923$ kg m^{-3}) exhibited a higher rigidity, while material HF ($E = 0.96$ MPa, $\rho_v = 704$ kg m^{-3}) was more flexible. The diameter, d, was fixed as 6 mm, while the vegetation lengths (l) were 9, 14 and 19 cm, resulting in the bending stiffness, EI, from 6.1×10^{-5} to 3.4×10^{-4} N m^2 and buoyancy parameter, B, from 0.21 to 11.64. In most cases, $Ca \gg B$, indicating that hydrodynamic drag dominated over the restoring force due to buoyancy. Therefore, buoyancy effects were considered negligible in this study. For comparison, wooden cylinders with identical geometrical parameters were used as rigid references. In total, 121 experimental cases with replicates were conducted under pure wave (PW), WCHC and WCLC conditions, covering a range of current-to-wave velocity ratio (β) from 0.19 to 1.56, Ca from 0.3 to 32 and L from 1.1 to 10.

2.2. *Velocity measurement*

Velocity measurements were conducted at mid-vegetation height using an acoustic Doppler velocimeter (ADV, Nortek) operating at a sampling rate of 50 Hz. The ADV was positioned at the centre of the truncated pyramid top in the x-direction and 5 cm from the edge in the y-direction. Phase (φ)-averaged velocity, $u_x(\varphi)$ and $u_y(\varphi)$, was calculated using the method developed by Lei & Nepf (2019*b*). The amplitude of the horizontal wave orbital velocity ($\tilde{u}_w$) and current velocity (u_c) were derived from $u(\varphi)$, as defined in (2.1) and (2.2), respectively. The measured velocities were subsequently used in force prediction. The wave excursion, A_w, was calculated by $A_w = \tilde{u}_w T/2\pi$.

$$\tilde{u}_w = \sqrt{2}\sqrt{\frac{1}{2\pi}\int_0^{2\pi} u_x^2(\varphi)\,\mathrm{d}\varphi}, \tag{2.1}$$

$$u_c = \frac{1}{2\pi}\int_0^{2\pi} u_y(\varphi)\,\mathrm{d}\varphi. \tag{2.2}$$

2.3. *Video processing and stem velocity*

Simultaneously with force measurements, underwater videos were recorded using two GoPro cameras to capture the motion of flexible stems. The cameras were mounted on metal plates positioned 1 m downstream in both the x- and y-directions to minimise flow

https://doi.org/10.1017/jfm.2025.10758 Published online by Cambridge University Press

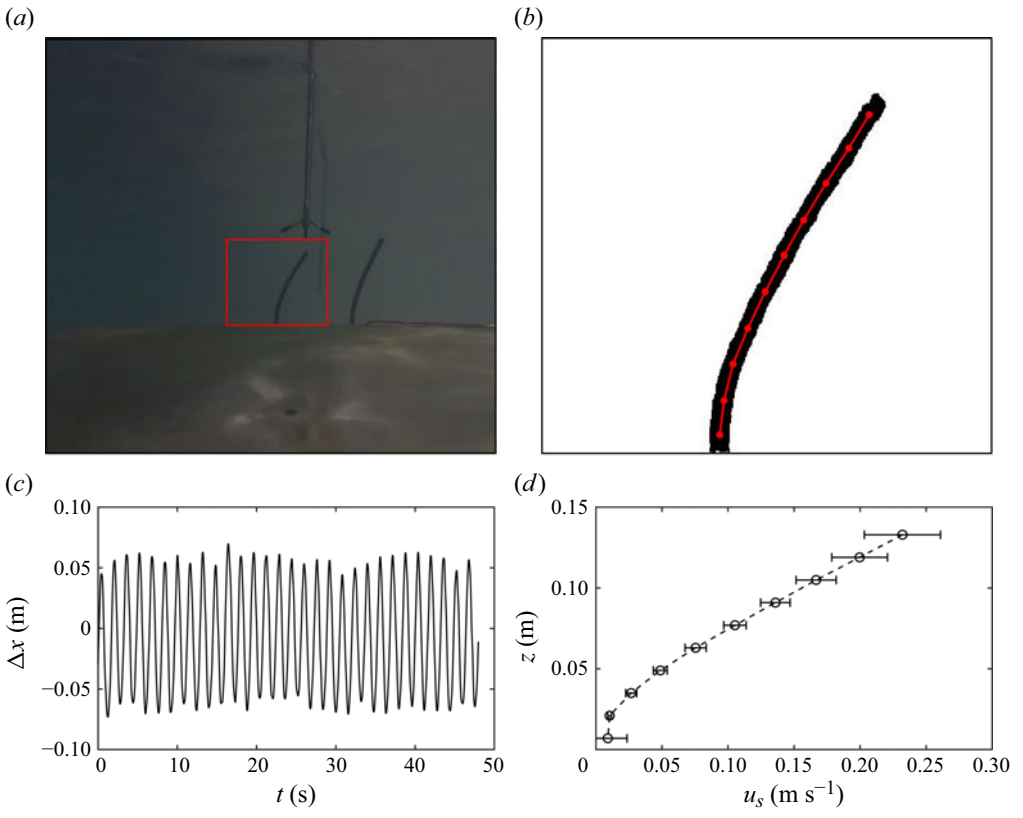


Figure 2. Example of the video processing workflow. (*a*) Raw video frame with a red rectangle highlighting the cropped region. (*b*) Processed frame showing the stem divided into 10 vertical segments, with red-filled circles marking the centre of mass of each segment. (*c*) Time series of the tip displacement. (*d*) Vertical velocity profile of the stem, with the error bars representing the standard deviation over 30 wave cycles.

interference. Videos were recorded over 10 wave cycles at a frame rate (f) of 60 fps. An example of the video processing workflow is shown in figure 2.

Video processing was performed using MATLAB's Image Processing Toolbox. Each video was converted to greyscale frame by frame, with the stem identified as the largest connected cluster of black pixels, while background noise was removed. The stem velocity was tracked along the stem by dividing it into 10 vertical segments. The centre of mass of each segment was determined by averaging the positions of black pixels. The travel distance (Δx) of each segment was then computed as the displacement of the centre of mass relative to its initial position in the absence of waves and currents. This displacement was converted to metres using a pixel-to-metre scale, derived from the known length of the stem. The stem velocity, u_s, was obtained by computing its temporal gradient along travel distance and then phase-averaged. The stem acceleration $\dot{u}_s$ was subsequently derived as the time derivative of velocity. The total centre-of-mass stem position was determined by averaging the positions of all black pixels, and the corresponding velocity $u_{s,c}$ was calculated from its displacement. To visualise the range of motion, edge detection was applied to each selected frame and the resulting binary images were stacked over one wave cycle to create a composite image. The tip excursion for each case was determined by measuring the distance between the leftmost and rightmost positions of the tip's centre. The uncertainty was evaluated by the standard deviation across 30 wave cycles. With

https://doi.org/10.1017/jfm.2025.10758 Published online by Cambridge University Press

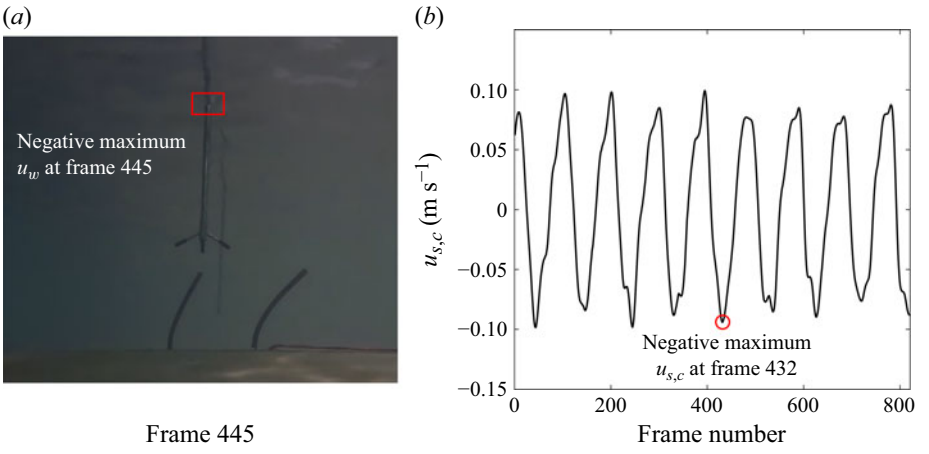


Figure 3. Example of phase shift estimation. (*a*) Frame 445, where the wave trough reaches the ADV rod, indicating the maximum negative wave velocity. (*b*) Corresponding frame 432, showing the maximum negative stem velocity.

an average scale of 0.3 mm pixel^{-1} and a time interval of 1/60 s between frames, the resolution of the stem velocity detected from the video is estimated to be 1.8 cm s^{-1}.

2.4. *Estimation of phase shift between stem and flow velocity*

We observed a phase shift ($\Delta\varphi$) between the stem and flow velocities. This phase shift results from the dynamic balance between the hydrodynamic forces and the restoring force due to stem stiffness. Accounting for this phase shift is essential to predict the total force on individual flexible stems. Although velocity measurements and video recordings were not synchronised, the phase shift was visually estimated by determining the frame difference (Δn) between the maximum flow velocity and the maximum stem velocity. The frame corresponding to the surface displacement peak or trough was identified by locating the highest or lowest interaction point between the water and the wave gauge or the supporting rod of the ADV (figure 3*a*), whichever provided a clearer reference. Since the surface displacement of the peak or trough corresponds to the maximum positive and negative flow velocity, this served as a reliable marker for determining the phase shift.

The frame in which the stem velocity reached its maximum was extracted from the velocity time series obtained through video processing (figure 3*b*). The phase shift for each case was calculated as the mean frame difference over 10 wave cycles. Additionally, since the ADV and wave gauge were positioned 10 cm upstream of the tracked stem, the phase difference due to this spatial offset was incorporated into the visually determined frame difference. Finally, the frame difference was converted to a phase shift using

$$\Delta\varphi = 2\pi \frac{\Delta n}{T} f, \tag{2.3}$$

where Δn is the frame difference and f is the frame rate of the camera.

2.5. *Force prediction*

The force prediction analysis was conducted to identify the key factors influencing total force on flexible stems, enabling a deeper understanding of the differences between flexible and rigid stem responses. It should be noted that only the force at x-direction was predicted and compared with the measured forces. The total force at x-direction (F_x),

https://doi.org/10.1017/jfm.2025.10758 Published online by Cambridge University Press

acting normally on an individual stem, comprises inertial and drag forces, as described by the Morison equation (Denny *et al.* 1998) and (2.4) in this study, where F_I, the inertial force, consists of the Froude–Krylov force (F_{VB}, also known as the virtual buoyancy force) and the added mass force (F_{AM}), while F_D is the drag force and $F_{I,s}$ is the stem inertia caused by the acceleration of the moving stem,

$$F_x = F_I + F_D - F_{I,b} = F_{VB} + F_{AM} + F_D - F_{I,s}. \tag{2.4}$$

Here, F_{VB} is given by

$$F_{VB}(\varphi) = \int_0^l \frac{1}{4}\rho\pi d^2 \dot{u}_x(\varphi)\,\mathrm{d}z, \tag{2.5}$$

where $\dot{u}_x$ denotes the acceleration of the wave velocity. Additionally, F_{AM} is trapezoidal integrated along the stem by

$$F_{AM}(\varphi) = \int_{z_1}^{z_{10}} \frac{1}{4}\rho\pi d^2 (C_m - 1)\dot{u}_{r,x}(\varphi, z_i)\,\mathrm{d}z, \tag{2.6}$$

where $\dot{u}_{r,x}$ denotes the acceleration of the relative velocity in the x- direction and C_m is the inertia coefficient. The vertical coordinate z was discretised into 10 segments with an increment of $10/l$, from $z_1 = l/20$ to $z_{10} = l - l/20$. The x-direction relative velocity at each segment, $u_{r,x}(\varphi, z_i)$, was defined as the difference between the flow velocity and the stem velocity. Because flow velocity varied little along the stem, it was assumed uniform and represented by the single-point measurement at mid-vegetation height, $u_x(\varphi)$. The stem velocity at z_i, $u_{s,i}$, was extracted from videos as described in § 2.3.

To align stem and flow velocity, the visually determined phase shift was applied. The ADV sampling rate was 50 Hz, while the video frame rate was 60 fps. To synchronise the datasets, the phase-averaged wave velocity was first interpolated to 60 Hz. The phase-averaged wave and stem velocity data were first arranged by phase (from peak to peak), and then $u_{s,i}$ was shifted forward by the identified phase shift.

Here, $u_{r,x}(\varphi, z_i)$ is given by

$$u_{r,x}(\varphi, z_i) = u_x(\varphi) - u_{s,i}(\varphi, z_i), \tag{2.7}$$

and F_D is calculated by

$$F_D(\varphi) = \int_{z_1}^{z_{10}} \frac{1}{2}\rho C_D\, d|u_r(\varphi, z_i)|u_{r,x}(\varphi, z_i)\,\mathrm{d}z, \tag{2.8}$$

where $u_r(\varphi, z_i)$ is the total relative velocity, representing the combination of relative velocity in the x- and y-directions. In the x-direction, $u_{r,x}$ is calculated by (2.7). In the y-direction, consistent with the uniform u_c assumption, only the mean velocity was considered, neglecting oscillatory components. Video analysis showed that the mean stem velocity $u_{s,y}$ was negligible, falling below the resolution of video-derived velocity measurements. Therefore, $u_{s,y}$ is assumed to be 0 and $u_{r,y}$ is expressed as

$$u_{r,y} = u_c - u_{s,y} = u_c. \tag{2.9}$$

Subequently, $u_r(\varphi, z_i)$ is given by

$$u_r(\varphi, z_i) = \sqrt{u_{r,x}^2(\varphi, z_i) + u_c^2}. \tag{2.10}$$

The inertia coefficient C_m and drag coefficient C_D are obtained by interpolating the relationships versus KC number, $KC = \tilde{u}_w T/d$, from Keulegan & Carpenter (1958) (their figures 10 and 11), an approach validated for orthogonal wave–current conditions with

https://doi.org/10.1017/jfm.2025.10758 Published online by Cambridge University Press

direct force measurements by Xu & Lei (2024*b*). Other studies have adopted the empirical relationships with Re (Petrolo *et al.* 2022; Zhu *et al.* 2023; Zhang *et al.* 2023).

Here, $F_{I,s}$ is calculated by

$$F_{I,s}(\varphi) = \int_{z_1}^{z_{10}} \frac{1}{4}\rho_b \pi d^2 \dot{u}_{s,i}(\varphi, z_i)\,\mathrm{d}z, \tag{2.11}$$

where $\dot{u}_{s,i}(\varphi, z_i)$ is the acceleration of the stem velocity in the x- direction.

2.6. *Scaling relationships for effective length*

2.6.1. *Previous scaling framework for effective length*

The scaling framework for effective length was developed to quantify the drag reduction due to plant reconfiguration in response to steady flow. The effective length was found to scale with two dimensionless parameters: the Cauchy number (Ca_c) and the buoyancy parameter (B). Here, Ca_c represents the ratio of hydrodynamic drag to the restoring force due to blade stiffness, while the buoyancy parameter quantifies the ratio of buoyancy to the restoring force (Luhar & Nepf 2011):

$$Ca_c = \frac{1}{2}\frac{C_D \rho b u_c^2 l^3}{EI}, \tag{2.12}$$

$$B = \frac{\Delta\rho g b d l^3}{EI}, \tag{2.13}$$

where ρ is the water density, b is the vegetation element (e.g. blade, stem) width, u_c is the steady current speed, l is the length, d is the thickness, $\Delta\rho$ is the density difference between water and vegetation, E is the Young's modulus, and I is the second moment of inertia. Previous studies indicate that B is small for common seagrass species such as *Thalassia testudinum*, *Posidonia oceanica* and *Zostera marina* ($B \leqslant 1.4$, see table 1 of Lei & Nepf (2016)). Within this range, B has a negligible effect on the posture of the vegetation.

In oscillatory flow, the wave Cauchy number, Ca_{pw}, is similarly expressed as

$$Ca_{pw} = \frac{1}{2}\frac{C_D \rho b u_w^2 l^3}{EI}, \tag{2.14}$$

where u_c is replaced by the wave velocity u_w. Zeller *et al.* (2014) observed that blade motion also depends on the ratio of wave excursion (A_w) to blade excursion, which represents the horizontal distances travelled by the wave and the blade within one wave period, respectively. To generalise this relationship, Luhar & Nepf (2016) introduced another dimensionless parameter, the length ratio (L):

$$L = \frac{l}{A_w} = \frac{2\pi l}{u_w T}. \tag{2.15}$$

Lei & Nepf (2019*a*) extended the scaling relationships for pure currents and pure waves to co-directional wave–current flows, and proposed the following equations to estimate l_e under various flow conditions:

$$\frac{l_e}{l} = \begin{cases} (1.09 \pm 0.07)(Ca_{pw} L)^{-0.25\pm0.02} & \text{for } u_c < 0.25u_w, \\ 0.9 Ca_{wc}^{-1/3} & \text{for } 0.25u_w \leqslant u_c < 2u_w, \\ 0.9 Ca_c^{-1/3} & \text{for } u_c \geqslant 2u_w, \end{cases} \tag{2.16}$$

where the subscripts 'pw', 'c' and 'wc' denote the pure wave, pure current and co-directional wave–current condition, respectively. The modified Ca in co-directional

https://doi.org/10.1017/jfm.2025.10758 Published online by Cambridge University Press

wave–current flows, Ca_{wc}, is given by

$$Ca_{wc} = \frac{1}{2}\frac{C_D \rho b l^3}{EI}\left(u_c^2 + \frac{1}{2}u_w^2\right), \tag{2.17}$$

where $(u_c^2 + 1/2u_w^2)$ is derived based on the equivalent time-averaged total drag force. It should be noted that the characteristic velocity scale u_w^2 in (2.14) is defined based on peak drag, instead of time-mean equivalent drag (Lei & Nepf 2019*a*). The characteristic velocity scale for Ca_{pw} defined based on the time-mean equivalent drag should be $1/2u_w^2$.

Luhar & Nepf (2016) noted that under inertia-dominated conditions, the force balance suggests that the effective length scales with CaL/KC rather than CaL, following a similar relation: $l_e/l \sim (CaL/KC)^{-1/4}$, where $KC = u_w T/d$ is the Keulegan–Carpenter number (Keulegan & Carpenter 1958) and d is the diameter of stems. Jacobsen *et al.* (2019) also highlighted the significance of CaL/KC, representing the inertia-to-stiffness ratio, in capturing the dynamics of flexible stems. In this study, CaL/KC was adopted as a key dimensionless parameter, and its effectiveness in characterising both stem motion and hydrodynamic forces was further evaluated.

2.6.2. *Hypotheses for scaling the effective length under orthogonal wave–current conditions*

We proposed a scaling framework for orthogonal wave–current conditions by reformulating the drag force expression. The scaling relationships in (2.16) were derived from a drag-dominated force balance. Because the total velocity entering the drag term differs when waves and currents are orthogonal, the drag expression must be modified accordingly.

We hypothesise that the drag force can be decomposed into x- and y-components. We consider several measure-time-averaged, root-mean-square (r.m.s.) and maximum-computed either from the total drag magnitude or from the directional components. For the following analysis, we adopt: (1) the time-averaged magnitude of the total drag and (2) the r.m.s. magnitude of the decomposed drag (C10). We choose the r.m.s. of the decomposed components to their time-averaged values because it yields a more compact analytical form. We do not use the maximum drag; justification is provided in § 4.1. Complete derivations for all measures (time-averaged total drag, time-averaged decomposed drag, r.m.s. decomposed drag and maximum decomposed drag) are given in Appendix C. Because the drag expression is modified under orthogonal wave–current forcing, the definition of the Cauchy number Ca must be adjusted accordingly, analogous to the modification in (2.17).

In this study, the scaling relationships for effective length under orthogonal wave–current flows were evaluated based on the total drag and also considered separately in the x- and y-directions. The expression for the time-averaged magnitude of the total drag (C7) suggests that the appropriate characteristic velocity for Ca_{wc} should be $(\sqrt{(1/2\tilde{u}_w^2 + u_c^2)})$. Thus, the definition of Ca_{wc} aligns with that used for co-directional wave–current flows (2.17). Here, $\boldsymbol{Ca}_{wc_{rms}}$ in each direction should be modified as

$$\boldsymbol{Ca}_{wc_{rms}} = \frac{1}{2}\frac{\rho C_D d l^3 \tilde{u}_w^2}{EI}\begin{bmatrix}\sqrt{\dfrac{4\beta^2+3}{8}} \\ \beta\sqrt{\beta^2+\dfrac{1}{2}}\end{bmatrix}, \tag{2.18}$$

where $\beta = u_c/\tilde{u}_w$ is the current-to-wave velocity ratio.

https://doi.org/10.1017/jfm.2025.10758 Published online by Cambridge University Press

In co-directional wave–current flows, stem motion is restricted by an additional current, resulting in a transition from wave-dominated to current-dominated scaling (2.16) as u_c increases. Under orthogonal wave–current flows, we hypothesise that the swaying motion in the x-direction remains insignificantly affected by the orthogonal current (verified in §§ 3.1 and 3.2) and the reconfiguration is still dependent on the wave excursion. Finally, the effective length, corresponding to the total drag, is assumed to scale with $Ca_{wc}L$ as

$$\frac{l_e}{l} = 1.1(Ca_{wc}L)^{-0.25}. \tag{2.19}$$

In the x- and y-directions, the effective lengths that correspond to r.m.s. drag are assumed to scale with $Ca_{wc_{rms,x}}L$ and $Ca_{wc_{rms,y}}$, respectively, as given by

$$\begin{aligned} \frac{l_{e,x}}{l} &= 1.1(Ca_{wc_{rms,x}}L)^{-0.25}, \\ \frac{l_{e,y}}{l} &= 0.9Ca_{wc_{rms,y}}^{-1/3}. \end{aligned} \tag{2.20}$$

2.6.3. *Force measurement and measured effective length ratio*

The total forces acting on the flexible stems were measured using submersible force transducers (FUTEK LSB210, with IP68 waterproof rating) with a measurement range from 0.001 to 10 N and a resolution of 0.001 N. Since these submersible sensors measure force in only one direction, two force transducers were installed perpendicular to each other to capture forces in both the x- and y-directions, with synchronised measurements. To facilitate accurate force measurements, a truncated pyramid (figure 1*a*) with eight inclined faces (1:5 slope) was designed as a platform for mounting the force transducers. The pyramid had a height of 0.1 m and a total length of 1.5 m. A customised metal holder securely attached each flexible stem to the force transducer using screws, ensuring rigid coupling between the stem and the transducer. Force measurements were conducted at a sampling rate of 1200 Hz over a 2-minute duration, capturing 60 to 100 wave cycles depending on the wave period. Simultaneously, surface displacement and flow velocities were recorded using a wave gauge and an ADV. Experiments were conducted to quantify background forces from the set-up without vegetation under various wave conditions. The recorded forces were negligible (of the order of 0.001 N) compared with those acting on the stems. Thus, flow-induced forces on the set-up itself were considered insignificant and omitted from further analysis. The uncertainties for force measurement were determined from replicate tests.

The measured total forces on the flexible stems were phase-averaged, $F(\varphi)$, following the method outlined by Lei & Nepf (2019*b*). The measured r.m.s. force at x-direction ($F_{rms,x}$), as described in (2.21), was used for comparison with predicted forces (calculated from § 2.5) in § 3.4.2.

$$\begin{aligned} F_{rms,x} &= \sqrt{\frac{1}{2\pi}\int_0^{2\pi} F_x^2(\varphi)\,\mathrm{d}\varphi}, \\ F_{rms,y} &= \sqrt{\frac{1}{2\pi}\int_0^{2\pi} F_y^2(\varphi)\,\mathrm{d}\varphi}. \end{aligned} \tag{2.21}$$

The time-averaged total force was calculated using

$$F_{mean,total} = \frac{1}{2\pi}\int_0^{2\pi} \sqrt{F_x^2(\varphi) + F_y^2(\varphi)}\,\mathrm{d}\varphi. \tag{2.22}$$

https://doi.org/10.1017/jfm.2025.10758 Published online by Cambridge University Press

These measured effective length ratios (l_e/l) were used to evaluate the validity of the scaling laws presented in (2.19) and (2.20). The effective length l_e is defined as the length of a rigid stem that experiences the same drag as a flexible stem of length l. Therefore, the measured l_e/l was determined by calculating the ratio of the measured force on a flexible stem to that on a rigid cylinder of identical geometry.

The measured l_e/l corresponds to time-average total force was defined by

$$\frac{l_e}{l} = \frac{F_{flexible,mean,total}}{F_{rigid,mean,total}}. \tag{2.23}$$

The measured effective length ratios corresponds to r.m.s. magnitude of decomposed forces were calculated by

$$\begin{aligned} \frac{l_{e,x}}{l} &= \frac{F_{flexible,rms,x}}{F_{rigid,rms,x}}, \\ \frac{l_{e,y}}{l} &= \frac{F_{flexible,mean,y}}{F_{rigid,mean,y}}. \end{aligned} \tag{2.24}$$

It should be noted that for evaluating the effective length in the y-direction, oscillation was neglected in accordance with the uniform u_c assumption and the mean force $F_{mean,y}$, defined as the mean of $F_y(\varphi)$, was used. The force measurements for flexible stems can be found in Appendix A, while the detailed data for rigid references can be found on Zenodo (Xu & Lei 2024*a*).

3. Results

3.1. *Stem motion*

Examples of stem motion extracted from video recordings are presented in figure 4. Stem motion is influenced by material properties, stem length and flow conditions. Within each row, the panels are arranged in ascending order of *CaL*. For stems of the same length, HF stems exhibit greater tip excursion than LF ones. For stems made of the same material, tip excursion increases with stem length. Comparing the first row figure 4(*a–e*) with the second row figure 4(*f–j*), the z-values under orthogonal wave–current flows are lower than those observed under pure wave conditions. In the wave propagation direction, the presence of an orthogonal current causes greater stem bending, particularly for HF stems. Under pure waves, the tip excursion follows a nearly two-dimensional trajectory, whereas under orthogonal wave–current conditions, the stem undergoes three-dimensional movements. In the current direction figure 4(*k–o*), the stem tends to bend more as *CaL* increases.

The asymmetric motion of the HF stems under pure waves, observed in figures 4(*d*) and 4(*e*), has also been reported in previous studies (Luhar & Nepf 2016; Zhu *et al.* 2020; Schaefer & Nepf 2024) and is attributed to stem movement in a spatially varying velocity field. Under pure waves, the stems exhibit a mean forward bending, but this asymmetric pattern was not observed under orthogonal wave–current conditions. This is attributed to the bending in the y-direction, which effectively increases the rigidity of the stem and constrains the motion in the x-direction.

3.2. *Range of motion*

The non-dimensional tip excursion of the stem is plotted as a function of *CaL* and *CaL*/*KC* in figures 5(*a*) and 5(*b*), respectively. Tip excursion quantifies how the stem tip moves with the flow. The dimensionless parameter *CaL*, adopted by Luhar & Nepf (2016),

https://doi.org/10.1017/jfm.2025.10758 Published online by Cambridge University Press

https://doi.org/10.1017/jfm.2025.10758 Published online by Cambridge University Press

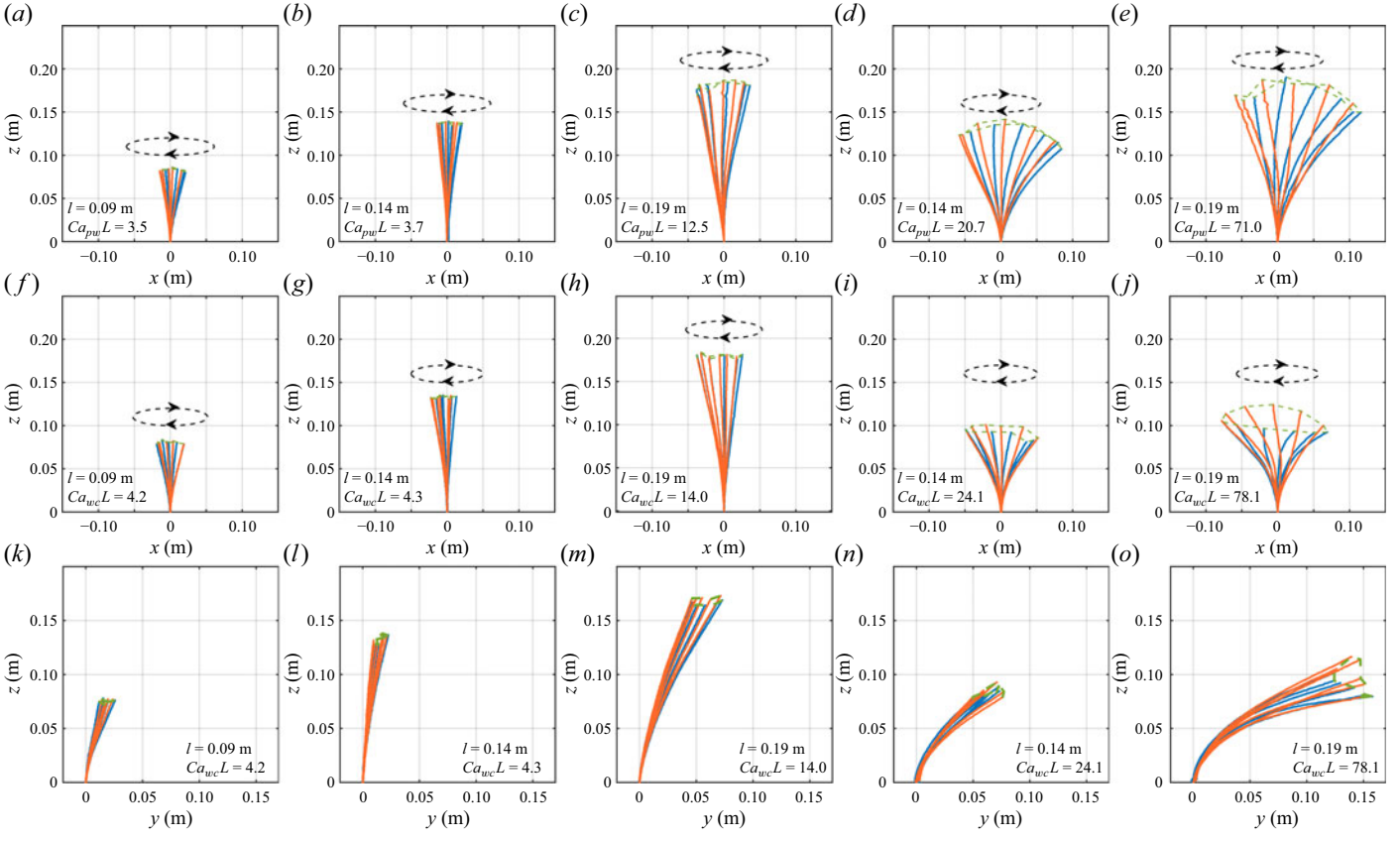


Figure 4. Examples of stem motion under wave conditions of $T = 1.6$ s and $H = 0.10$ m. (*a–e*) Stem motion in the wave propagation direction under pure waves. (*f–j*) Stem motion in the wave propagation direction under WCHC conditions. (*k–o*) Stem motion in the current direction under WCHC conditions. Each column corresponds to stems with the same properties. Orange lines represent frames with positive velocity, while blue lines indicate frames with negative velocity. Black dashed ellipses show the wave horizontal excursion, $2A_w$, at the mid-vegetation height.

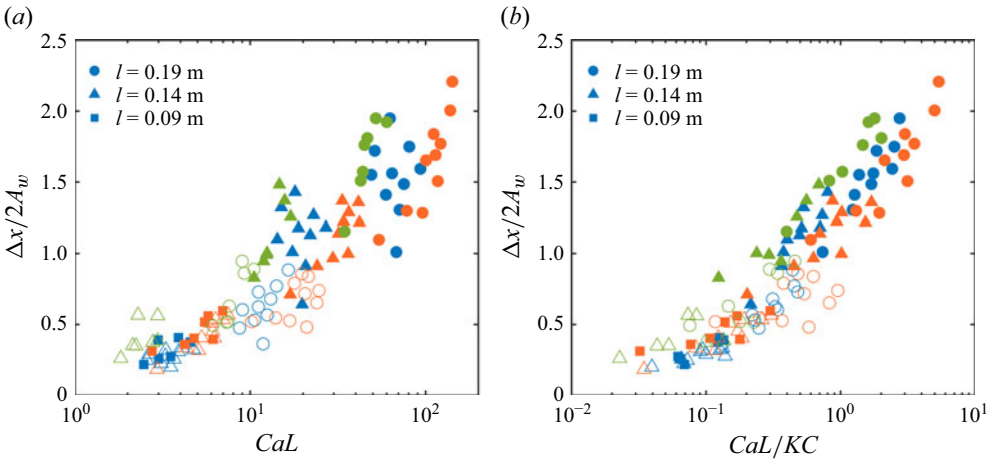


Figure 5. Tip excursion normalised by wave excursion as a function of (*a*) *CaL* and (*b*) *CaL*/*KC*. Marker shape indicates stem length. PW, WCHC and WCLC are shown in blue, orange and green, respectively. Closed and open markers represent HF and LF stems, respectively. Standard deviations are less than 10 % and smaller than the symbol size, and thus not displayed.

represents the ratio of drag force to blade stiffness, while *CaL*/*KC*, introduced by Jacobsen *et al.* (2019), represents the ratio of inertial force to blade stiffness. As expected, tip excursion increases with *CaL* and *CaL*/*KC*. The presence of an orthogonal current does not significantly affect the horizontal range of stem motion, as tip excursions under PW, WCHS and WCLS follow similar trends with *CaL* and *CaL*/*KC*. For stems with shorter lengths, higher elastic moduli and under mild waves (i.e. $CaL < 1$), their motion closely resembles that of nearly rigid stems, consistent with the findings of Luhar & Nepf (2016) and Jacobsen *et al.* (2019).

In figure 5(*a*), data points tend to cluster based on stem length, particularly for $CaL > 20$, where tip excursion varies significantly despite similar *CaL* values. However, in figure 5(*b*), the clustering of data points was improved by plotting against *CaL*/*KC*, suggesting that *CaL*/*KC* better captures the range of stem motion than *CaL* alone. This finding aligns with Jacobsen *et al.* (2019) and Leclercq & De Langre (2018). Tip excursion reaches a value of approximately 2.0, consistent with Jacobsen *et al.* (2019) within a similar *CaL* and *CaL*/*KC* range. Leclercq & De Langre (2018) also reported a comparable maximum value, though their y-axis variable, $\Delta x/A_w$, is twice the magnitude of the corresponding values in this study.

3.3. *Phase shift*

Stem velocity and flow velocity are not necessarily in phase, as theoretically described by Mullarney & Henderson (2010) and observed in the field by Bradley & Houser (2009). Accounting for this phase shift is essential for accurately simulating stem motion and predicting the forces acting on vegetation. For nearly rigid vegetation, the stem velocity leads the surrounding water velocity by 90°. In contrast, highly flexible vegetation moves in phase with the water flow. The phase shift arises from the interplay between the restoring force due to stiffness and the hydrodynamic forces exerted by the water. For vegetation with intermediate flexibility, the phase shift falls within the range of 0° to 90°. Understanding this phase shift is crucial for capturing the dynamic response of flexible vegetation under wave–current interactions.

https://doi.org/10.1017/jfm.2025.10758 Published online by Cambridge University Press

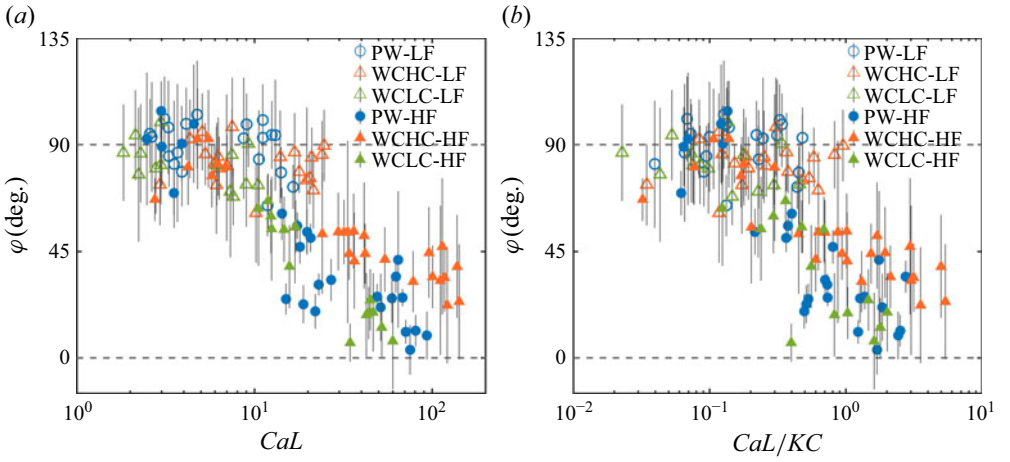


Figure 6. Phase shift between the water particle and the stem as a function of (*a*) CaL and (*b*) CaL/KC. The uncertainties come from the standard deviation across 10 wave cycles.

The phase shift, determined from video recordings, is presented in figure 6 as a function of CaL and CaL/KC. The phase shift patterns are consistent across different flow conditions, and generally decrease with increasing CaL and CaL/KC. When $CaL < 10$ and $CaL/KC < 0.2$, stems exhibit a phase shift close to 90°, behaving similarly to rigid structures. Some values exceeding 90° may be attributed to uncertainties in visually counting phase differences. In this study, stems moved nearly in phase with the water when $CaL > 70$ and $CaL/KC > 1$, consistent with the findings of Jacobsen *et al.* (2019). Additionally, the presence of an orthogonal current did not affect the observed phase shift. The measured phase shift was subsequently applied to align the stem velocity with the flow velocity for accurate force prediction on the flexible stems.

In the near-bed portion of a flexible stem, phase shift is 90°. The phase shift decreases to zero within the elastic boundary layer (Mullarney & Henderson 2010). Jacobsen *et al.* (2019) observed a constant phase shift along the stem when $CaL < 20$ and $CaL/KC < 0.5$, with stem motion following a single-mode response. At higher CaL, inflection points appear along the stem, resembling motion mode 1, 2 and 3 defined in Mullarney & Henderson (2010). Under these conditions, different points along the stems do not reach maximum bending simultaneously. However, in this study, we assume a uniform phase shift along the stem length. This assumption is justified for LF stems, where the measured phase shift averages 82°, closely aligning with the 90° shift characteristic of the near-bed rigid layer. For HF stems, the near-bed rigid layer is much thinner than the elastic boundary layer, as seen in figure 4. Above the near-bed boundary layer, inflection points were not observed and the stems remained straight, exhibiting the mode 0 behaviour defined by Mullarney & Henderson (2010), where all points along the stem reach maximum bending simultaneously. Given these observations, assuming a uniform phase shift along the stem length is a reasonable simplification in this study.

3.4. *Force prediction*

3.4.1. *Velocities and the predicted forces*

Examples of velocities and their corresponding predicted forces are shown in figure 7. Relative velocity reduction is a key factor in the force reduction in flexible vegetation compared with rigid vegetation. Bradley & Houser (2009) observed decreased wave

https://doi.org/10.1017/jfm.2025.10758 Published online by Cambridge University Press

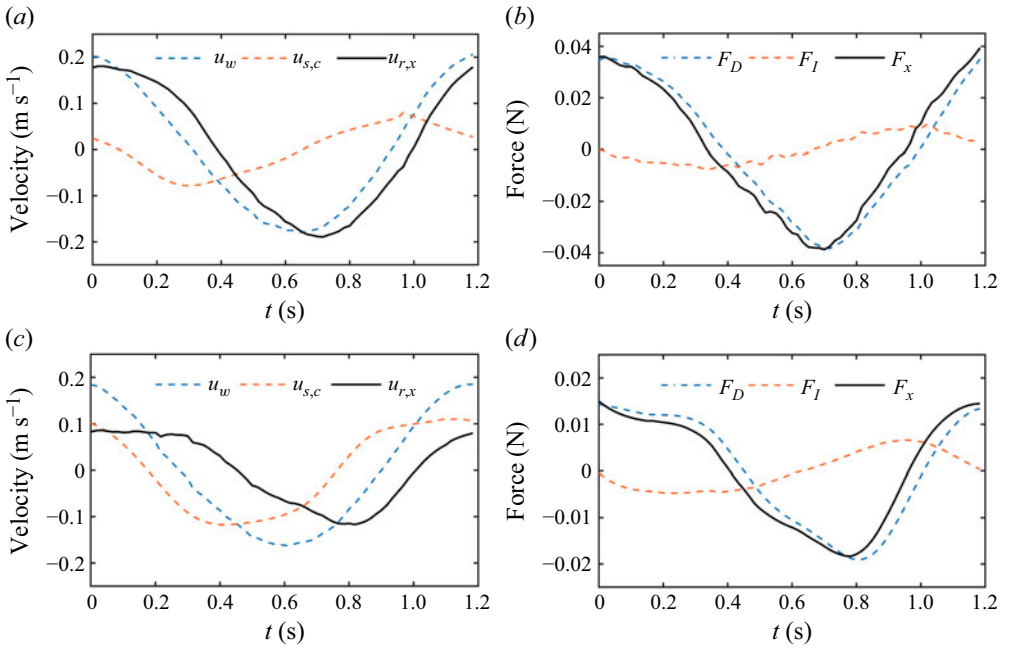


Figure 7. Wave velocity, stem velocity and relative velocity for (*a*) LF and (*c*) HF stems. Drag force, inertial force and total force in x-direction for (*b*) LF and (*d*) HF stems. Both cases are under WCHC conditions with $T = 1.2$ s and $H = 0.10$ m.

energy attenuation by flexible vegetation due to its relative motion between the real seagrass blades and oscillatory flows. In figure 7(*a*), the flow velocity and stem velocity are in quadrature. The centre-of-mass stem velocity, $u_{s,c}$, was used to illustrate the differences between HF and LF stems. The maximum $|u_{s,c}|$ of LF stems is 7.9 cm s^{-1} due to the relatively small range of motion. With minimal influence from $u_{s,c}$, the relative velocity u_r closely follows u_w in magnitude, with a slight phase shift.

In contrast, in figure 7(*c*), $u_{s,c}$ and u_w are nearly in phase, with a phase difference as small as 0.18π. The maximum $|u_{s,c}|$ of HF stems reaches 10.9 cm s^{-1}, reducing the magnitude of u_r to approximately half of $|u_w|$. In this scenario, the total force remains primarily governed by drag. Under these conditions, the measured $F_{x,rms}$ for LF and HF stems corresponds to 75 % and 35 % of $F_{rigid,x,rms}$, respectively, highlighting the significant force reduction in flexible vegetation.

3.4.2. *Force prediction with different assumptions*

The comparison between predicted and measured forces is shown in figure 8. Overall, LF stems experience higher forces than HF stems due to their greater rigidity. A comparison of the left and right columns of figure 8 reveals that incorporating phase shift improves the accuracy of force predictions. Specifically, when the counted phase shift is included, the root-mean-squared error (RMSE) between predicted and measured forces decreases from 0.0060 N to 0.0038 N (see figures 8*a* and 8*b*).

Under orthogonal wave–current conditions (figures 8*c* and 8*d*), force predictions using in-phase assumption overestimated the measured forces, with an RMSE of 0.0035 N. Including the phase-shift effect improved the overestimation but yielded the same RMSE of 0.0035 N. This discrepancy arises because flexible stems bend in the current direction, reducing their frontal area normal to the horizontal wave velocity. To account for this

https://doi.org/10.1017/jfm.2025.10758 Published online by Cambridge University Press

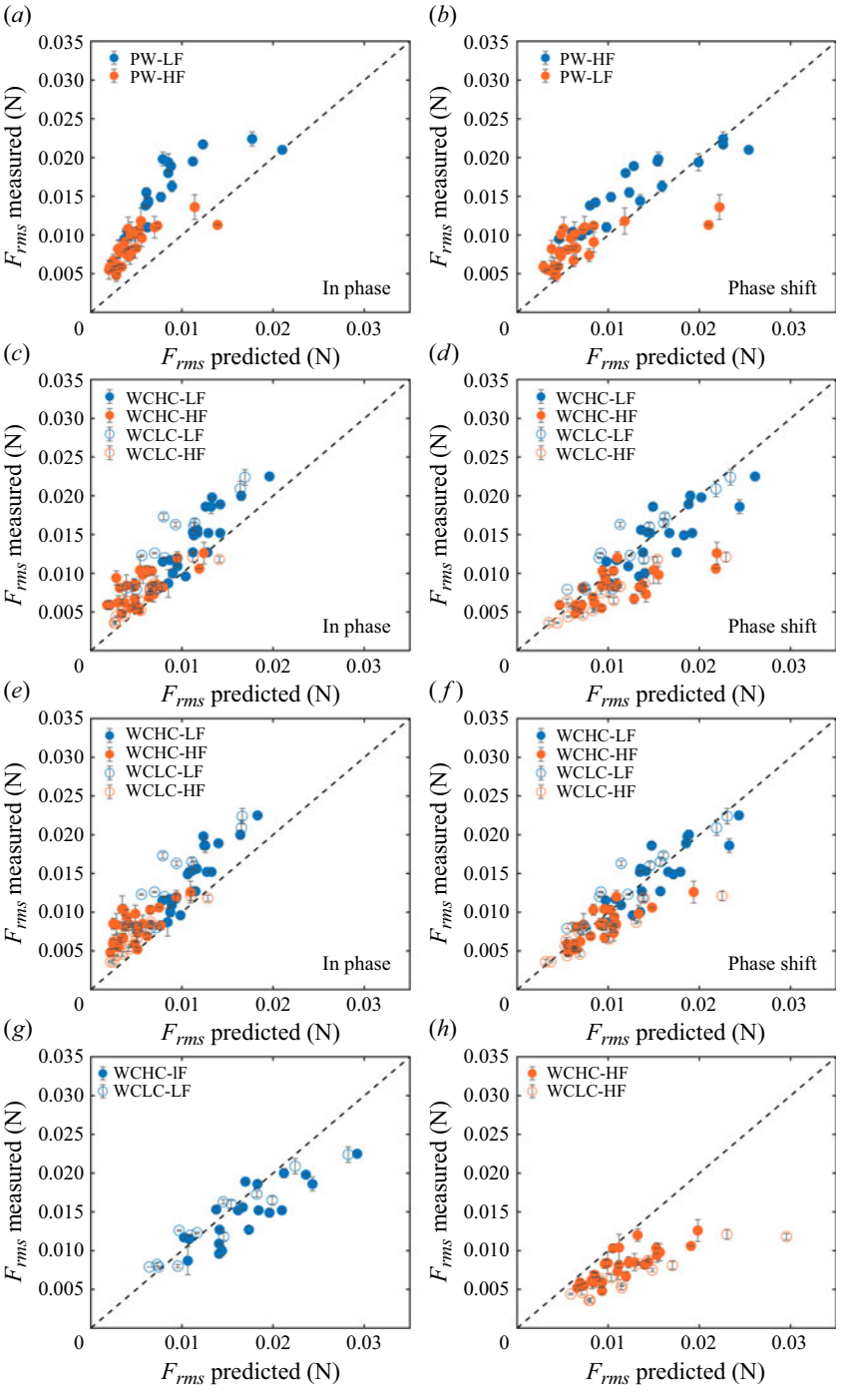


Figure 8. Comparison between measured and predicted forces. The left column assumes water and stem velocity are in phase, while the right column incorporates the exact phase shift. (*a*,*b*) Forces under pure waves. (*c*,*d*) Forces under orthogonal wave–current flows using the original vegetation length l. (*e*,*f*) Forces under orthogonal wave–current flows with the deflected vegetation length l_d. (*g*,*h*) Forces under orthogonal wave–current flows considering solely l_d, treating flexible stems as rigid. Uncertainties arise from force measurement replicates.

https://doi.org/10.1017/jfm.2025.10758 Published online by Cambridge University Press

effect, the deflected height, l_d, was measured from video recordings in y-direction. By replacing l with l_d in the force prediction equations, the corrected predicted forces (figure 8*f*) align well with the measured values, reducing the RMSE from 0.0035 N to 0.0025 N.

With the inclusion of relative velocity, phase shift and deflection effects, our force prediction model demonstrates strong agreement with the measured values. Additionally, force predictions were compared using a simplified approach that considers only deflection while ignoring changes in relative velocity. This approach treats flexible vegetation as rigid stems of length of l_d. The results for LF and HF stems are shown in figures 8(*g*) and 8(*h*), respectively. Although this simplified approach works better for LF stems, generating an RMSE of 0.0031 N, it strongly overestimates the forces on HF stems, with an RMSE of 0.0054 N, resulting in an overestimation of wave attenuation by highly flexible vegetation such as seagrass. This is because less flexible vegetation behaves more like rigid stems, exhibiting relatively low stem velocity. In contrast, highly flexible vegetation responds more actively to oscillatory flows, making the difference between flow velocity and stem velocity more pronounced.

In summary, accurately predicting forces on flexible vegetation requires accounting for both relative velocity and frontal area reduction. Under pure wave conditions, the reduction in relative velocity plays a dominant role in force reduction compared with rigid vegetation. However, under orthogonal wave–current conditions, both reduced frontal area and relative velocity contribute to force reduction. Furthermore, the strong agreement between predictions and measurements suggests that drag and inertia coefficients can be reliably determined from their relationship with the *KC* number (Keulegan & Carpenter 1958).

3.4.3. *Inertia and drag*

Inertial forces were found to contribute significantly to the total force acting on flexible vegetation within the tested β range from 0.19 to 1.56 in this study. Previous studies have assessed the relative importance of inertial forces using the *KC* number. However, since Keulegan & Carpenter (1958) originally developed this parameter for rigid cylindrical structures in oscillatory flows, *KC* is primarily applicable to rigid vegetation. In this study, we found the significance of inertial effects varies with flexibility. To capture this variability, we compare the ratio of predicted inertial force to total force as a function of CaL/KC in figure 9.

Inertial contributions increase with increasing CaL/KC for both pure wave and orthogonal wave–current conditions. This suggests that inertial forces become more pronounced for shorter wave periods, higher stem flexibility and longer stems. For stems of the same length, HF stems experience a larger inertial impact than LF stems because the latter are more rigid and therefore subject to higher drag forces.

Under orthogonal wave–current conditions (figure 9*b*), trends differ between the WCLC and WCHC cases. In WCHC, inertial forces increase gradually with CaL/KC, reaching up to 29 %. In contrast, WCLC follows a pattern similar to that of pure waves, with inertial contributions increasing rapidly with CaL/KC to 73 %. The presence of a strong orthogonal current (β from 0.65 to 1.56) appears to weaken the relative significance of inertia. This is because the increased total flow velocity enhances drag, while the virtual buoyancy force (F_{VB}) and the added mass force (F_{AM}) are not influenced.

Inertial forces consist of the F_{VB}, F_{AM} and stem inertia ($F_{I,s}$). The stem inertia, which scales with the acceleration of the stem itself, is relatively small in this study. The relative importance of F_{VB} and F_{AM} depends on the flow conditions. Here, F_{VB} becomes more

https://doi.org/10.1017/jfm.2025.10758 Published online by Cambridge University Press

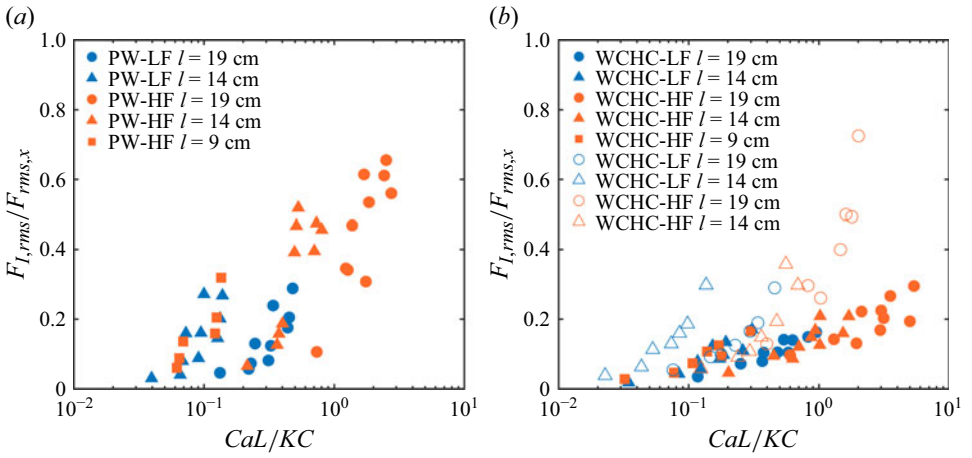


Figure 9. Predicted inertial forces normalised by the total force under (*a*) pure wave and (*b*) orthogonal wave–current conditions. Circle, triangle and square markers represent stem length of 19, 14 and 9 cm, respectively. Uncertainties can come from measured $\tilde{u}_w \sin(\varphi)$ and video-derived stem velocity.

important when the wave period and wave height are smaller and the magnitude of acceleration is relatively large compared with the wave velocity. In contrast, F_{AM}, which scales with relative acceleration, contributes more substantially when wave velocities are higher.

In general, inertial forces require particular attention in flow conditions characterised by shorter wave periods and highly flexible vegetation. Previous studies often neglected these effects, as they primarily examined thin rectangular plates (e.g. 0.4 mm by Luhar & Nepf (2016), and 0.1 mm by Lei & Nepf (2019*a*) and Schaefer & Nepf (2024)), resulting in significantly lower mass compared with the cylindrical stems examined in this study. Consequently, inertial forces play a more prominent role here.

4. Discussion

4.1. *Force metric selection for effective length analysis*

The choice of force metric affects both the expression of the characteristic velocity scale in *Ca* and the resulting estimation of effective length. The concept of effective length was initially introduced for unidirectional flow, where a flexible stem of length l experiences the same drag force as a rigid stem of the same length (Luhar & Nepf 2011). In oscillatory flows, different definitions of effective length have been proposed.

Luhar & Nepf (2016) extended the effective length framework to oscillatory flow using the r.m.s. force, which effectively represents the magnitude of force over one wave cycle. They also showed that the scaling law for pure waves remains valid when using the maximum force. Lei & Nepf (2019*a*) later calculated effective length based on time-mean force in co-directional wave–current flows. Caution is needed when using the maximum force within a wave cycle, as inertial forces can introduce a phase shift between the maximum total force and the maximum drag force (figure 7). When inertial forces are negligible, the maximum total force can be considered equivalent to the maximum drag force. Since inertial contributions in this study are non-negligible, the maximum total force cannot be used. Instead, we examine the effective length using both the time-mean total force and the r.m.s. force, as shown in figure 10.

https://doi.org/10.1017/jfm.2025.10758 Published online by Cambridge University Press

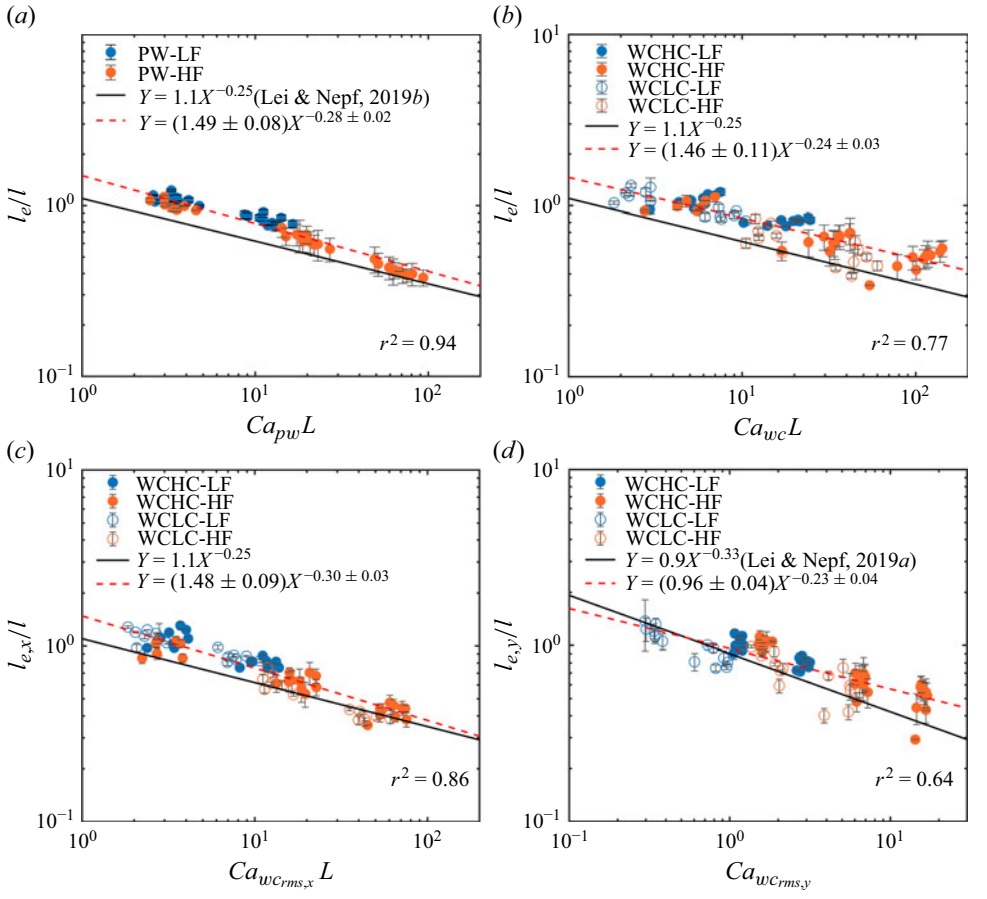


Figure 10. (*a*) Effective length under pure waves versus $Ca_{pw}L$. (*b*) Effective length from time-mean total force versus $Ca_{wc}L$ under orthogonal wave–current flows. (*c*) Effective length from r.m.s. force in the x-direction versus $Ca_{wc_{rms,x}}L$. (*d*) Effective length from r.m.s. force in the y-direction versus $Ca_{wc_{rms,y}}$. Red dashed lines represent fitted formulae with the adjusted r^2 shown in the lower right corner of each panel, while black solid lines indicate the hypothesised scaling laws ((2.19) for panel *b* and (2.20) for panels *c* and *d*). Uncertainties of the measured force arise from replicate tests.

4.2. *Comparison of scaling laws under pure waves*

Figure 10(*a*) compares the normalised measured effective length, calculated from the r.m.s. force, as a function of $Ca_{pw}L$ for pure waves. All experimental cases in this study fall within the small deflection range ($L > 1$), where the effective length is expected to scale as $l_e/l \sim Ca_{pw}L^{-0.25}$(Luhar & Nepf 2016; Lei & Nepf 2019*b*). The power of $Ca_{pw}L$, fitted as 0.28 ± 0.02, aligns closely with the theoretical value of 0.25. However, the scaling coefficient, 1.49 ± 0.08, is 35 % higher than 1.1, which was fitted by Lei & Nepf (2019*b*).

The scaling coefficient is affected by the aspect ratio of the stem cross-section. Previous studies modelled flexible vegetation using thin rectangular sheets with significantly smaller aspect ratio, such as 0.095 for foam blades and 0.02 for HDPE blades by Luhar & Nepf (2016), and 0.01 for LDPE blades by Lei & Nepf (2019*b*). In contrast, cylindrical silicone rubber stems with an aspect ratio of 1 were used in this study. The smaller aspect ratio will lead to significantly lower volume, leading to negligible inertial effects. However, the higher-volume cylindrical stems used in this study produced non-negligible inertial

https://doi.org/10.1017/jfm.2025.10758 Published online by Cambridge University Press

contributions. As shown in figure 9(*a*), inertial forces account for an average of 25 % of the total force, thus increasing the total force beyond the drag component alone.

Luhar & Nepf (2016) reported that the scaling for pure waves underestimated the effective lengths of HDPE stems, attributing this discrepancy to vortex shedding when the drag force and stem stiffness were of comparable magnitude, i.e. $Ca \sim O(1)$. A similar phenomenon may explain the higher measured effective lengths in this study. Here, Ca is of the order of $O(1)$ for all LF stems and HF stems with a length of 9 cm. However, when $Ca > 10$ (HF stems with lengths of 14 and 19 cm), the effective lengths converge to the expected scaling law (black solid line in figure 10*a*).

4.3. *Comparison of scaling laws under combined wave–current flows*

Figure 10(*b*) compares the measured effective length, calculated from the time-mean total force, as a function of $Ca_{wc}L$. The fitted scaling exponent (-0.24 ± 0.02) agrees with the hypothesised value of –0.25 in (2.19). The fitted scaling coefficient (1.46 ± 0.11) is larger than the expected value of 1.1. This finding is similar to pure wave results (figure 10*a*) and is attributed to greater inertial contributions from the larger material aspect ratio used here. These results support using $Ca_{wc}L$, with $u_c^2 + 1/2u_w^2$ being the characteristic velocity scale in Ca_{wc}, as the appropriate scaling parameter under orthogonal wave–current flows. This scaling differs from that used for co-directional wave–current flows, where Ca_{wc} alone is applied when $0.25 < \beta < 2$ in (2.16). This difference highlights a key physical insight, showing that with an orthogonal current within the β range from 0.19 to 1.56 in this study, the combined forcing is wave-dominated, whereas under co-directional conditions, it can be current-dominated.

The consistent alignment of data from under both WCHC and WCLC conditions demonstrates that the hypothesised scaling relationship (2.19) holds for a β range from 0.19 to 1.56. When β approaches 0 and current velocity becomes negligible, the characteristic velocity in Ca_{wc} reduces to $1/2u_w^2$, representing the time-mean magnitude of drag under pure wave conditions. Conversely, when β becomes large and the current velocity dominates, the characteristic velocity approaches u_c^2, which corresponds to the definition of Ca_c (2.12). We therefore recommend adopting the definition of Ca_{wc} (2.17) for co-directional and orthogonal wave–current flows, as well as pure waves and pure currents, to provide a unified dimensionless scaling for effective length.

Figures 10(*c*) and 10(*d*) further evaluate the effective length in the orthogonal wave–current conditions along the x- and y-directions, respectively, where the effective lengths were derived from the r.m.s. forces in each direction. In the x-direction, the $l_{e,x}$ exhibits a similar trend to figure 10(*a*), converging towards the solid line when $Ca_{wc_{rms,x}} > 10$. In the y-direction, the current is expected to remain the dominant driver of the flexible stem motion, leading to a scaling parameter solely with $Ca_{wc_{rms,y}}$, independent of L. However, the fitted power of $Ca_{wc_{rms,y}}$ is –0.23 ± 0.04, larger than the expected (–0.33), indicating that forces in the current direction were notably influenced by the presence of orthogonal waves. The $l_{e,y}/l$ at $Ca_{wc_{rms,y}}$ in the range of 0.3–2 fluctuates around 1, indicating behaviour similar to rigid stems. This result is consistent with Luhar & Nepf (2011), who found the stiff-to-flexible transition to occur when $Ca < 2$.

The effective length was also evaluated using $Ca_{wc}L/KC$. However, the data exhibited significant scatter, especially for the combined wave–current condition. As noted by Luhar & Nepf (2016), the effective length is expected to scale with CaL/KC under inertia-dominated conditions. In contrast, for the experimental cases in this study, although inertial forces contributed to the total force, hydrodynamic drag remained the dominant component, explaining the absence of a clear scaling relationship with $Ca_{wc}L/KC$.

https://doi.org/10.1017/jfm.2025.10758 Published online by Cambridge University Press

Physical parameters		Strap-leaf seagrass*	*Amphibolis antarctica* stem**	Pneumatophore roots***	Model in this study
Shape		Rectangular sheet	Cylinder	Cone	Cylinder
Width, b (mm)		5.83 ± 4.38	1–3	2–15	6
Thickness, d (mm)		0.43 ± 0.41	1–3	2–15	6
Length, l (cm)		30.49 ± 21.73	20–50	5–25	9, 14, 19
Modulus, E (MPa)		114.22 ± 90.77	160.56 ± 169.83	800	0.96(HF); 5.36(LF)
Wave velocity, u_w (m s^{-1})		0.3–1.3	0.3–1.3	0.3–1.3	0.12–0.3
EI (10^{-6} N m^2)		0.88–7.9	125–260	630–30 000	61(HF); 340(LF)
L		0.5–12.5	1–12.5	0.3–6.3	1.0–8.4
$\beta = 0$	Ca_{wc}	20–2.3×10^4	1.6–53.6	2.2×10^{-4}–1.3	0.5–32
	$Ca_{wc}L$	10–2.8×10^5	1.6–670	6.6×10^{-5}–8.2	2.5–93.3
	l_e/l	< 0.46	1.3–0.29	> 0.88	1.2–0.38
$\beta = 1$	Ca_{wc}	60–6.7×10^4	5.0–161	6.7×10^{-4}–4	1.5–96
	$Ca_{wc}L$	30–8.3×10^5	5.0–2×10^3	2.0×10^{-4} –25	1.5–806
	l_e/l	< 0.35	< 0.99	> 0.66	1.3–0.28
$\beta = 2.7$	Ca_{wc}	300–3.4×10^5	25–820	3.4×10^{-3}–20	7.3–466
	$Ca_{wc}L$	150– 4.2×10^6	25–1×10^4	1.0×10^{-3}–120	7.3–3.9×10^3
	l_e/l	< 0.23	< 0.66	> 0.44	0.9–0.19

Table 1. Comparison between the physical parameters in natural environments and this study.

*de los Santos *et al.* (2016)
**de los Santos *et al.* (2016); Womersley (1984)
***Zhang *et al.* (2015).

4.4. *Application of effective length to real flexible vegetation*

To estimate the effective length of real vegetation, we compiled data from prior studies on wave–current conditions, and on the mechanical and morphological properties of several species. Using these data, we calculated the corresponding CaL values under natural conditions, with and without currents, and predicted the associated effective length ratios, as summarised in table 1.

When waves approach the shoreline at an oblique angle, they generate longshore currents. However, relatively few field studies have quantified longshore current velocities. Galvin (1967) summarised early measurements, reporting a mean velocity of 0.08 m s^{-1}. Sherman (1988) recorded longshore currents at five field sites in Sandy Hook, New Jersey, with a mean of 0.23 ± 0.29 m s^{-1}. On the central Atlantic coast of Florida, Burnette & Dally (2017) reported a 10-year dataset showing strong seasonal and climatic variability, with monthly averaged velocities ranging from 0 to 0.15 m s^{-1} and 2-hour averaged velocities generally below 0.4 m s^{-1}. Almar *et al.* (2016) conducted experiments at a 10-m depth off the Gulf of Guinea, West Africa, reporting surf-zone longshore currents of 0.4–0.8 m s^{-1}. Field measurements by Li *et al.* (2020) in the southern East China Sea during summer to autumn revealed a significant influence of tides and seasonality, with residual currents ranging from 0.1 to 0.5 m s^{-1}. In summary, longshore current velocities vary widely depending on location, season and climate, with typical values ranging from 0 to 0.8 m s^{-1}. Nearshore short waves typically exhibit wave periods of 1−5 s and wave heights of 3−20 cm (Wiberg *et al.* 2019; Lee *et al.* 2021). Given a nearshore wave velocity range of 0.3–1.3 m s^{-1}, the corresponding β range in natural coastal environments typically spans from 0 to approximately 2.7.

Seagrasses exhibit a wide range of E, from 0.1 to 2.4 GPa across different species (Lei & Nepf 2016; de los Santos *et al.* 2016; Vettori & Marjoribanks 2021). de los Santos

https://doi.org/10.1017/jfm.2025.10758 Published online by Cambridge University Press

et al. (2016) conducted a comprehensive analysis of the mechanical and morphological properties of 22 species of tropical and temperate seagrasses. Globally, seagrasses exhibit three distinct growth forms. The form commonly modelled by thin sheets consists of strap-like leaves arising directly from the rhizome, such as *Zostera marina, Thalassia hemprichii, Posidonia oceanica*. Another type consists of short strap-like leaves arising from a vertical stem, predominantly found in southern and western Australia, e.g. *Amphibolis antarctica* (commonly known as wire weed). de los Santos *et al.* (2016) reported that the mechanical properties of these stems differ significantly from their leaves, exhibiting greater strength, stiffness and extensibility, making them more resilient under varying hydrodynamic forces. The third growth form consists of plants with paired oval leaves attached to the rhizome via a petiole. These species are typically short and exhibit morphologies distinct from the flexible cylinder model used in this study.

The vegetation model used in this study can be considered a simplification of *Amphibolis antarctica*, representing only the stem and ignoring the leaves. Additionally, the model is also representative of mangrove pneumatophore roots. Mangrove pneumatophore roots have been reported to exhibit a cone-shaped appearance with diameters ranging from 2 to 15 mm and an E of approximately 0.8 GPa (Zhang, Chua & Cheong 2015), resulting in a bending stiffness (EI) from 6.3×10^{-4} to $3 \times 10^{-2}\,\mathrm{Nm}^2$, which closely resembles the LF stems ($EI = 3.4 \times 10^{-4}\,\mathrm{Nm}^2$) in this study. The EI of stems of *Amphibolis antarctica* were calculated to range from 1.25×10^{-4} to $2.6 \times 10^{-4}\,\mathrm{Nm}^2$, also comparable to the LF stems and slightly larger than that of the HF stems ($EI = 6.1 \times 10^{-5}\,\mathrm{Nm}^2$) tested in this study.

To isolate the influence of longshore currents, the wave velocity u_w was fixed to $0.3\,\mathrm{m\,s}^{-1}$, while the current velocity varied from 0 to $0.8\,\mathrm{m\,s}^{-1}$. Mangrove pneumatophore roots were simplified as cylindrical structures with diameters ranging from 2 to 15 mm for the calculations. For strap-like seagrass, l_e/l was calculated using the scaling law for pure waves ((2.16) when $u_c = 0\,\mathrm{m\,s}^{-1}$), based on a fitted range of $Ca_{wc}L$ from $O(10^{-1})$ to $O(10^5)$. For *Amphibolis antarctica* stems and pneumatophore roots, l_e/l was predicted using the fitted scaling shown in figure 10(*b*), with a fitting range of $Ca_{wc}L$ from $O(10^0)$ to $O(10^2)$.

This study examined $Ca_{wc}L$ values ranging from $O(10^0)$ to $O(10^2)$, due to the fixed morphology and flexibility of the stem material. However, natural vegetation spans a much broader range of $Ca_{wc}L$ values. When orthogonal longshore currents are considered, the predicted l_e/l values become markedly smaller. Strap-like seagrasses can experience $Ca_{wc}L$ from $O(10^1)$ to $O(10^6)$, with l_e/l generally below 0.46. Notably, when $Ca_{wc}L > 10^3$, the effective length no longer follows the scaling law but instead tends to stabilise around 0.1 (see figure 5 of Lei & Nepf 2019*b*), suggesting that the scaling framework (2.16) may not be applicable beyond this range. *Amphibolis antarctica* stems exhibit $Ca_{wc}L$ from $O(10^1)$ to $O(10^4)$ with the predicted l_e/l values ranging from 0.29 to 1.3. For mangrove pneumatophore roots, $Ca_{wc}L$ spans from $O(10^{-5})$ to $O(10^2)$, with predicted l_e/l exceeding 0.44. The predicted l_e/l values are much greater than 1 when $Ca_{wc}L \ll O(10^0)$, which is not physically realistic. When the stems are relatively short and stiff ($Ca_{wc}L < 1$), although the scaling law ((2.16) when $u_c = 0\,\mathrm{m\,s}^{-1}$) may yield effective lengths greater than 1, the actual effective length should be around 1 due to their near-rigid behaviour. While both this study and Luhar & Nepf (2016) observed l_e/l can slightly exceed 1 due to vortex shedding, flexible stems are unlikely to experience forces several times larger than those acting on rigid stems.

The scaling framework of effective length physically links the hydrodynamic forces in flexible structures to the corresponding forces on rigid structures with the same morphology. By knowing the morphological and mechanical properties of the structures,

https://doi.org/10.1017/jfm.2025.10758 Published online by Cambridge University Press

this approach provides a practical way to estimate forces (Sun *et al.* 2024). Moreover, it can be extended beyond force prediction for vegetation alone, serving as a foundation for other physical models, such as wave energy decay models, to quantify wave energy dissipation by flexible vegetation (Luhar *et al.* 2017; Lei & Nepf 2019*b*; Beth Schaefer & Nepf 2022).

5. Conclusion

This study addresses a research gap by investigating the reconfiguration and hydrodynamic forces of flexible stems under orthogonal wave–current conditions. We extended and validated existing scaling laws for effective length to orthogonal conditions by modifying the definitions of Ca, and we introduced a new method to predict the total force on flexible stems. A total of 121 experimental cases were conducted in a wave–current basin, varying stem elasticity, stem length, wave periods, wave heights and current speeds. Stem motion was analysed using video recordings, from which the centre of mass velocities were extracted to calculate the relative velocity between the flow and the stems. The results showed that the phase shift between flow velocity and stem velocity decreases from 90° to 0° as CaL increases. The close agreement between the measured and predicted forces confirms that the extracted stem velocity provides a reliable basis for computing the relative velocity. By incorporating stem velocity, phase shift and deflection in height, the predicted forces aligned well with the experimental measurements.

Inertial effects contributed significantly to the total force, especially for more flexible stems, attributed to the larger material aspect ratio used here relative to previous research. Consistent with our hypotheses, under orthogonal wave–current flows, the effective length associated with the total force scales as $Ca_{wc}L^{-0.25}$. For cylindrical stems, the scaling coefficient exceeded values reported previously, reflecting the additional inertial contribution in this study. In the decomposed directions, the effective length in the wave-propagation direction scales with $Ca_{wc_{rms,x}}L$, whereas in the current direction, it scales with $Ca_{wc_{rms,y}}$. Although the non-dimensional parameter CaL/KC better describes tip motion, it showed limited correlation with effective length because it primarily reflects inertial forces rather than drag-induced reconfiguration. By integrating previous studies on effective length under unidirectional currents, pure waves and co-directional wave–current flows with the present orthogonal case, we expand the effective-length framework, making it more comprehensive and applicable to complex real-world conditions.

This study provides valuable datasets on hydrodynamic forces and stem motion under orthogonal wave–current conditions, which remain under-studied. However, the experiments employed simple cylindrical flexible stems and did not include torsional effects. Future work should explore stems with more complex morphologies that better represent natural vegetation. In addition, more research is needed on the interactions between stems within vegetated meadows under oblique wave–current conditions to better quantify their influence on hydrodynamic forces and wave attenuation.

Acknowledgements. The authors thank Mr Shaja Khan for his assistance and the Central Workshop of NUS for manufacturing the load cell holder and the truncated pyramid. Artificial intelligence tools (ChatGPT, OpenAI) were used solely to improve the clarity and grammar of the text. No AI tools were used for data analysis, interpretation or generation of scientific content.

Funding. This study is supported by the National University of Singapore (NUS) start-up grant under A-0009542-02-00 and by the MOE Tier1 grant under A-8001202-00-00.

Declaration of interests. The authors report no conflict of interest.

Data availability statement. The data supporting the findings of this study have been uploaded to figshare by Xu & Lei (2025).

https://doi.org/10.1017/jfm.2025.10758 Published online by Cambridge University Press

Appendix A. Table of experimental cases

Material	T (s)	a_w (cm)	u_w (m s^{-1})	KC	C_D	C_M	Ca_{pw}	L	$Ca_{pw}L$	F_{rms} (mN)	l_e/l
LF	1.2	2.4	0.118	23.5	1.6	1.1	1.32	8.48	11.15	10.6 ± 0.4	0.915 ± 0.032
$l = 0.19$ m,	1.2	4.1	0.166	31.6	1.5	1.3	2.25	6.29	14.12	15.5 ± 0.6	0.847 ± 0.033
$B = 0.52$	1.2	5.0	0.202	38.3	1.4	1.5	3.18	5.19	16.48	19.8 ± 0.9	0.779 ± 0.035
	1.4	2.5	0.118	26.7	1.5	1.2	1.21	7.47	9.03	9.9 ± 0.4	0.867 ± 0.038
	1.4	3.3	0.158	34.5	1.5	1.4	1.93	5.76	11.13	14.4 ± 0.8	0.812 ± 0.043
	1.4	4.1	0.200	42.7	1.4	1.6	2.81	4.67	13.10	19.4 ± 1.1	0.752 ± 0.042
	1.6	3.2	0.142	35.3	1.5	1.4	1.54	5.63	8.69	11.0 ± 0.6	0.885 ± 0.047
	1.6	4.2	0.188	46.1	1.4	1.7	2.45	4.32	10.60	16.3 ± 0.7	0.848 ± 0.035
	1.6	5.1	0.238	56.7	1.3	1.8	3.56	3.51	12.51	21.7 ± 0.5	0.792 ± 0.020
	2.0	4.9	0.305	89.3	1.2	2.3	5.32	2.23	11.84	21.0 ± 0.0	0.763 ± 0.000
LF	1.2	3.0	0.122	23.7	1.6	1.1	0.52	6.26	3.28	9.9 ± 0.1	1.226 ± 0.017
$l = 0.14$ m,	1.2	4.0	0.161	31.1	1.5	1.3	0.88	4.69	4.13	14.2 ± 0.5	1.076 ± 0.035
$B = 0.21$	1.2	4.8	0.199	37.3	1.4	1.4	1.21	3.92	4.75	18.0 ± 0.2	0.995 ± 0.011
	1.4	2.5	0.118	26.4	1.5	1.2	0.48	5.55	2.64	9.5 ± 0.2	1.054 ± 0.023
	1.4	3.3	0.161	34.9	1.5	1.4	0.78	4.21	3.30	13.8 ± 0.1	1.037 ± 0.007
	1.4	4.1	0.206	43.1	1.4	1.6	1.16	3.37	3.91	18.9 ± 0.3	1.032 ± 0.019
	1.6	3.3	0.144	35.5	1.5	1.4	0.63	4.11	2.58	10.4 ± 0.1	1.148 ± 0.007
	1.6	4.3	0.189	45.5	1.4	1.6	0.97	3.21	3.11	14.9 ± 0.6	1.101 ± 0.041
	1.6	5.3	0.239	56.1	1.3	1.8	1.42	2.59	3.68	19.5 ± 0.3	1.012 ± 0.017
	2.0	5.4	0.302	89.2	1.2	2.3	2.18	1.62	3.53	22.4 ± 0.9	1.110 ± 0.045
HF	1.2	2.9	0.115	22.8	1.6	1.0	7.45	8.42	62.54	4.8 ± 0.8	0.414 ± 0.072
$l = 0.19$ m,	1.2	4.1	0.165	32.2	1.5	1.3	13.17	6.13	80.67	7.3 ± 1.1	0.398 ± 0.060
$B = 11.64$	1.2	4.9	0.208	38.6	1.4	1.5	18.38	5.08	93.35	9.6 ± 1.1	0.378 ± 0.041
	1.4	2.4	0.124	27.7	1.5	1.2	7.01	7.32	51.29	5.2 ± 0.8	0.455 ± 0.070
	1.4	3.3	0.172	36.7	1.4	1.4	11.64	5.53	64.34	7.4 ± 0.8	0.418 ± 0.045
	1.4	4.1	0.211	44.4	1.4	1.6	16.74	4.49	75.16	10.1 ± 0.9	0.391 ± 0.034
	1.6	3.3	0.144	35.7	1.5	1.4	8.80	5.57	49.04	6.0 ± 1.0	0.486 ± 0.084
	1.6	4.1	0.193	46.7	1.4	1.7	13.84	4.29	59.35	8.3 ± 1.3	0.434 ± 0.066
	1.6	5.0	0.247	57.8	1.3	1.9	20.57	3.45	71.02	11.0 ± 1.4	0.402 ± 0.052
	2.0	5.4	0.314	92.6	1.2	2.3	31.68	2.15	68.05	11.3 ± 0.0	0.412 ± 0.000
HF	1.2	3.0	0.115	22.5	1.6	1.0	2.80	6.44	18.01	5.5 ± 1.2	0.674 ± 0.146
$l = 0.14$ m,	1.2	4.0	0.165	31.4	1.5	1.3	4.89	4.70	22.98	7.8 ± 1.6	0.595 ± 0.121
$B = 4.66$	1.2	4.9	0.207	38.4	1.4	1.5	7.03	3.84	27.00	10.1 ± 1.6	0.556 ± 0.087
	1.4	2.5	0.128	28.4	1.5	1.2	2.79	5.41	15.05	5.9 ± 0.7	0.659 ± 0.076
	1.4	3.3	0.169	36.8	1.4	1.4	4.58	4.12	18.84	8.2 ± 1.1	0.617 ± 0.085
	1.4	4.2	0.210	44.4	1.4	1.6	6.57	3.35	21.98	10.8 ± 1.5	0.589 ± 0.082
	1.6	3.3	0.144	35.6	1.5	1.4	3.43	4.16	14.27	6.7 ± 0.8	0.737 ± 0.087
	1.6	4.4	0.191	46.2	1.4	1.7	5.45	3.19	17.39	9.1 ± 1.3	0.677 ± 0.096
	1.6	5.3	0.241	56.8	1.3	1.8	8.04	2.57	20.70	11.8 ± 1.7	0.613 ± 0.087
	2.0	5.3	0.312	91.9	1.2	2.3	12.26	1.61	19.77	13.6 ± 1.6	0.676 ± 0.080
HF	1.2	2.9	0.113	22.1	1.6	1.0	0.69	4.32	2.99	5.5 ± 0.1	1.124 ± 0.023
$l = 0.09$ m,	1.2	4.1	0.165	31.1	1.5	1.3	1.28	3.05	3.90	8.1 ± 0.0	0.993 ± 0.005
$B = 1.24$	1.2	5.1	0.203	37.5	1.4	1.4	1.82	2.51	4.56	10.7 ± 0.0	0.938 ± 0.000
	1.6	3.4	0.146	35.8	1.5	1.4	0.94	2.62	2.48	5.9 ± 0.2	1.072 ± 0.029
	1.6	4.4	0.194	46.7	1.4	1.7	1.49	2.02	3.01	8.3 ± 0.2	1.013 ± 0.024
	1.6	5.3	0.240	57.0	1.3	1.8	2.12	1.66	3.52	11.2 ± 0.3	0.943 ± 0.022
	2	5.2	0.271	87.6	1.2	2.3	3.13	1.06	3.32	12.3 ± 0.5	0.967 ± 0.042

Table 2. Experimental cases under pure waves with $\beta = 0$.

https://doi.org/10.1017/jfm.2025.10758 Published online by Cambridge University Press

Material	T (s)	a_w (cm)	$\tilde{u}_w$ (m s^{-1})	β	KC	C_D	C_M	Ca_{wc}	L	$F_{mean,total}$ (mN)	l_e/l
LF	1.2	3.4	0.118	1.28	25.9	1.6	1.1	3.07	8.02	20.1 ± 0.8	0.827 ± 0.032
$l = 0.19$ m,	1.2	4.8	0.166	1.01	34.2	1.5	1.3	3.39	6.32	23.1 ± 0.2	0.813 ± 0.007
$B = 0.52$	1.2	5.6	0.202	0.85	41.0	1.4	1.4	3.67	5.36	25.5 ± 0.8	0.817 ± 0.026
	1.4	3.6	0.118	1.43	29.1	1.5	1.2	3.39	7.08	21.1 ± 1.0	0.852 ± 0.040
	1.4	4.7	0.158	1.13	38.1	1.5	1.4	3.72	5.50	24.8 ± 0.1	0.820 ± 0.002
	1.4	5.7	0.200	0.92	47.5	1.4	1.6	3.90	4.59	28.6 ± 0.3	0.761 ± 0.007
	1.6	2.8	0.142	1.44	36.1	1.5	1.3	3.42	6.14	20.1 ± 0.1	0.832 ± 0.003
	1.6	3.6	0.188	1.11	45.7	1.4	1.5	3.45	4.86	22.0 ± 0.4	0.826 ± 0.015
	1.6	4.2	0.238	0.89	55.7	1.3	1.7	3.33	4.19	22.6 ± 0.0	0.766 ± 0.000
	2.0	4.1	0.305	0.69	87.0	1.3	2.1	3.94	2.58	29.4 ± 0.0	0.798 ± 0.000
LF	1.2	3.5	0.122	1.33	24.5	1.6	1.1	1.22	6.16	20.2 ± 0.9	1.198 ± 0.054
$l = 0.14$ m,	1.2	4.9	0.161	0.99	32.9	1.5	1.4	1.41	4.49	24.0 ± 0.0	1.162 ± 0.000
$B = 0.21$	1.2	6.0	0.199	0.87	39.1	1.4	1.4	1.51	3.95	25.8 ± 0.6	1.102 ± 0.024
	1.4	3.5	0.118	1.47	26.9	1.5	1.2	1.27	5.51	21.8 ± 0.2	1.147 ± 0.011
	1.4	4.5	0.161	1.18	35.4	1.5	1.4	1.42	4.30	24.4 ± 0.5	1.022 ± 0.019
	1.4	5.4	0.206	0.96	42.9	1.4	1.5	1.47	3.59	27.4 ± 0.5	0.961 ± 0.016
	1.6	2.8	0.144	1.50	33.8	1.5	1.3	1.31	4.76	20.4 ± 0.6	1.125 ± 0.036
	1.6	3.7	0.189	1.15	43.4	1.4	1.5	1.37	3.71	21.9 ± 0.4	1.070 ± 0.020
	1.6	4.3	0.239	0.94	51.6	1.4	1.7	1.36	3.18	23.0 ± 0.7	1.047 ± 0.033
	2.0	3.9	0.302	0.68	85.1	1.3	2.1	1.52	1.93	26.7 ± 1.5	0.948 ± 0.052
HF	1.2	3.3	0.115	1.31	26.4	1.6	1.1	17.68	8.02	13.7 ± 1.5	0.565 ± 0.061
$l = 0.19$ m,	1.2	4.8	0.165	1.03	34.4	1.5	1.3	19.07	6.38	14.6 ± 1.6	0.515 ± 0.057
$B = 11.64$	1.2	5.2	0.208	0.89	37.0	1.5	1.4	19.59	5.67	15.3 ± 2.0	0.490 ± 0.064
	1.4	3.6	0.124	1.52	27.7	1.5	1.1	17.98	7.68	13.5 ± 1.9	0.543 ± 0.076
	1.4	4.4	0.172	1.15	38.5	1.5	1.4	19.88	5.73	15.3 ± 2.4	0.506 ± 0.079
	1.4	5.6	0.211	0.95	47.3	1.4	1.6	20.83	4.83	15.9 ± 2.0	0.423 ± 0.053
	1.6	2.7	0.144	1.47	37.4	1.5	1.3	18.46	6.36	12.8 ± 2.2	0.530 ± 0.092
	1.6	3.6	0.193	1.14	49.5	1.4	1.5	19.42	4.95	13.3 ± 2.1	0.501 ± 0.080
	1.6	4.3	0.247	0.89	60.0	1.3	1.8	18.61	4.19	13.1 ± 2.2	0.444 ± 0.074
	2.0	4.1	0.314	0.65	90.2	1.3	2.1	21.06	2.57	12.6 ± 0.0	0.343 ± 0.000
HF	1.2	3.5	0.115	1.32	24.4	1.6	1.1	6.81	6.09	11.6 ± 1.6	0.691 ± 0.096
$l = 0.14$ m,	1.2	5.1	0.165	1.01	35.7	1.5	1.3	8.16	4.47	13.7 ± 2.2	0.663 ± 0.107
$B = 4.66$	1.2	5.9	0.207	0.89	38.3	1.4	1.4	8.21	4.07	14.3 ± 2.5	0.612 ± 0.107
	1.4	3.5	0.128	1.56	27.4	1.5	1.1	7.41	5.66	13.3 ± 2.9	0.697 ± 0.151
	1.4	4.5	0.169	1.18	36.4	1.5	1.3	7.86	4.33	14.3 ± 2.7	0.599 ± 0.113
	1.4	5.4	0.210	1.02	45.5	1.4	1.5	8.78	3.63	15.5 ± 2.9	0.544 ± 0.100
	1.6	2.8	0.144	1.52	35.7	1.5	1.3	7.60	4.76	12.2 ± 1.7	0.674 ± 0.094
	1.6	3.7	0.191	1.17	47.1	1.4	1.5	8.13	3.64	13.5 ± 2.3	0.662 ± 0.111
	1.6	4.3	0.241	0.94	53.6	1.4	1.7	7.54	3.20	13.5 ± 2.4	0.614 ± 0.110
	2.0	4.0	0.312	0.70	83.7	1.3	2.1	8.73	1.94	15.4 ± 1.9	0.546 ± 0.069
HF	1.2	3.2	0.113	1.31	23.3	1.6	1.1	1.75	4.00	11.1 ± 0.8	1.124 ± 0.077
$l = 0.09$ m,	1.2	4.9	0.165	0.96	33.8	1.5	1.3	1.98	2.90	12.9 ± 0.3	0.971 ± 0.020
$B = 1.24$	1.2	5.7	0.203	0.86	39.8	1.5	1.4	2.11	2.61	14.0 ± 0.1	0.931 ± 0.004
	1.6	2.8	0.146	1.51	34.4	1.5	1.3	2.02	3.03	11.9 ± 0.0	1.066 ± 0.002
	1.6	3.6	0.194	1.13	44.7	1.4	1.5	2.00	2.39	12.8 ± 1.0	1.060 ± 0.084
	1.6	4.3	0.240	0.96	55.0	1.4	1.6	2.05	2.05	13.4 ± 0.6	0.987 ± 0.043
	2	4.2	0.271	0.68	85.3	1.3	2.1	2.17	1.27	15.6 ± 0.2	0.932 ± 0.014

Table 3. Experimental cases under WCHC conditions with current velocity $u_c = 0.16$ m s^{-1}.

https://doi.org/10.1017/jfm.2025.10758 Published online by Cambridge University Press

Material	T (s)	a_w (cm)	$\tilde{u}_w$ (m s^{-1})	β	KC	C_D	C_M	Ca_{wc}	L	$F_{mean,total}$ (mN)	l_e/l
LF	1.2	2.6	0.100	0.63	19.7	1.7	0.9	0.76	9.97	9.1 ± 0.3	0.879 ± 0.033
$l = 0.19$ m,	1.2	4.0	0.141	0.47	27.3	1.5	1.2	1.26	7.08	14.3 ± 0.1	0.929 ± 0.004
$B = 0.52$	1.2	5.3	0.182	0.41	35.4	1.5	1.4	1.95	5.47	18.2 ± 0.4	0.816 ± 0.016
	1.6	2.8	0.120	0.64	32.2	1.5	1.3	0.98	6.22	10.5 ± 0.5	0.973 ± 0.043
	1.6	3.7	0.158	0.50	42.0	1.4	1.5	1.48	4.73	13.7 ± 0.9	0.864 ± 0.059
	1.6	4.6	0.193	0.40	51.8	1.3	1.8	2.01	3.87	17.4 ± 0.6	0.837 ± 0.031
	2.0	4.5	0.242	0.25	80.7	1.3	2.2	2.82	2.46	22.5 ± 1.1	0.862 ± 0.043
LF	1.2	2.8	0.104	0.68	21.8	1.6	1.0	0.34	7.08	9.0 ± 1.2	1.277 ± 0.171
$l = 0.14$ m,	1.2	4.3	0.144	0.47	28.4	1.5	1.2	0.53	5.10	13.6 ± 0.7	1.197 ± 0.060
$B = 0.21$	1.2	5.2	0.180	0.38	34.9	1.4	1.4	0.76	4.08	16.9 ± 0.1	1.064 ± 0.008
	1.6	2.9	0.120	0.68	31.2	1.5	1.3	0.40	4.60	9.9 ± 0.3	1.309 ± 0.037
	1.6	3.7	0.155	0.49	40.4	1.4	1.6	0.57	3.54	13.0 ± 0.1	1.181 ± 0.005
	1.6	4.7	0.195	0.39	51.5	1.3	1.8	0.81	2.82	16.5 ± 0.1	1.137 ± 0.004
	2.0	4.5	0.245	0.25	80.4	1.2	2.2	1.15	1.79	20.5 ± 0.4	1.036 ± 0.022
HF	1.2	3.0	0.112	0.51	23.1	1.6	1.0	4.82	8.92	5.7 ± 0.4	0.552 ± 0.038
$l = 0.19$ m,	1.2	4.3	0.144	0.46	29.1	1.5	1.2	7.37	6.89	7.7 ± 0.3	0.503 ± 0.022
$B = 11.64$	1.2	4.7	0.186	0.41	37.2	1.4	1.4	11.38	5.35	9.9 ± 0.6	0.447 ± 0.029
	1.6	2.9	0.119	0.71	30.7	1.5	1.3	5.64	6.27	6.6 ± 0.6	0.614 ± 0.057
	1.6	3.5	0.156	0.55	42.6	1.4	1.6	8.29	4.80	7.5 ± 1.0	0.470 ± 0.061
	1.6	4.5	0.193	0.41	51.8	1.3	1.8	11.19	3.88	8.1 ± 0.3	0.389 ± 0.013
	2.0	4.6	0.261	0.19	86.9	1.2	2.3	17.66	2.29	11.4 ± 0.4	0.435 ± 0.017
HF	1.2	3.0	0.106	0.60	21.3	1.6	1.0	1.83	6.94	5.6 ± 0.2	0.793 ± 0.024
$l = 0.14$ m,	1.2	4.2	0.120	0.58	28.2	1.5	1.2	2.29	6.28	7.6 ± 0.2	0.669 ± 0.022
$B = 4.66$	1.2	5.0	0.161	0.47	35.9	1.5	1.4	3.64	4.60	8.4 ± 0.0	0.532 ± 0.003
	1.6	2.8	0.153	0.51	33.0	1.5	1.3	3.18	3.73	6.3 ± 0.4	0.841 ± 0.054
	1.6	3.5	0.137	0.59	42.1	1.4	1.6	2.70	4.12	7.8 ± 0.3	0.709 ± 0.031
	1.6	4.6	0.174	0.46	52.4	1.3	1.8	3.88	3.20	9.4 ± 0.3	0.648 ± 0.019
	2.0	4.3	0.227	0.33	84.9	1.2	2.2	5.79	1.97	12.0 ± 0.8	0.605 ± 0.040

Table 4. Experimental cases under WCLC conditions with current velocity $u_c = 0.06$ m s^{-1}.

Appendix B. Evaluation of linear stem velocity assumption

Stem velocities were obtained by dividing the stem into 10 segments and differentiating the centre-of-mass displacement of each segment over time. However, this segmentation and integration process is time-consuming and impractical for field applications, because complete stem motion, particularly near the base, is often not fully captured. To address this, we evaluated the linear velocity assumption, in which a linear velocity profile along the stem was assumed. Specifically, u_s was interpolated based on the assumptions that $u_s = 0$ at $z = 0$ m (stem base) and $u_s = 2u_{s,c}$ at $z = l$, where $u_{s,c}$ represents the velocity at the total centre of mass of the stem ($z = l/2$). Figure 11 compares the vertical velocity profiles derived from full-stem tracking against those obtained using the linear assumption. The comparison indicates that the linear assumption underestimates velocities near the tip and overestimates them near the base. The maximum deviation is approximately 40 % at the tip, as shown in figure 11(*d*).

To assess the impact of these velocity discrepancies on force prediction, force predictions were calculated separately using velocities derived from the linear assumption and full-stem tracking methods with the original stem length l, and compared in figure 12. For pure wave conditions (figure 12*a*) and orthogonal wave–current flows (figure 12*b*), the resulting RMSE values are 0.0019 N and 0.0023 N, respectively. These results indicate that, within the CaL range examined, the linear-velocity assumption produces acceptable

https://doi.org/10.1017/jfm.2025.10758 Published online by Cambridge University Press

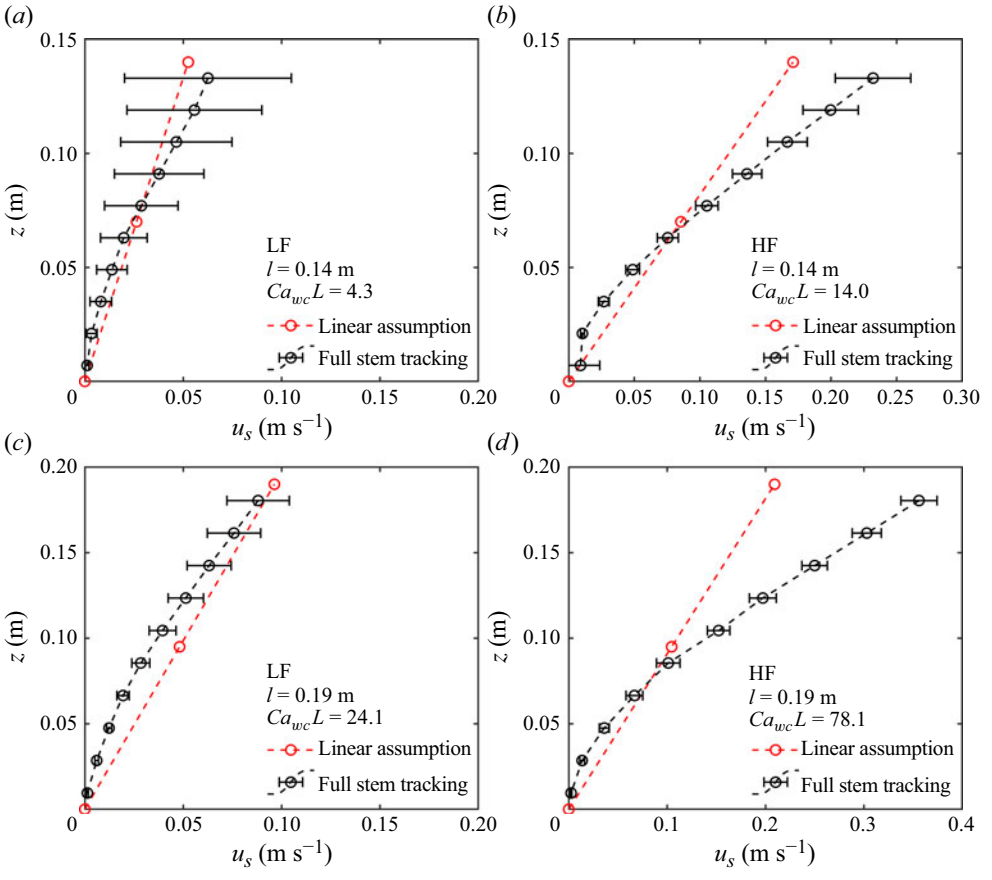


Figure 11. Comparison of along-stem velocities from full-stem tracking and linear assumption under WCHC conditions ($T = 1.6$ s, $H = 0.10$ m). Panels (*a–d*) correspond to panels (*g–j*) in figure 4.

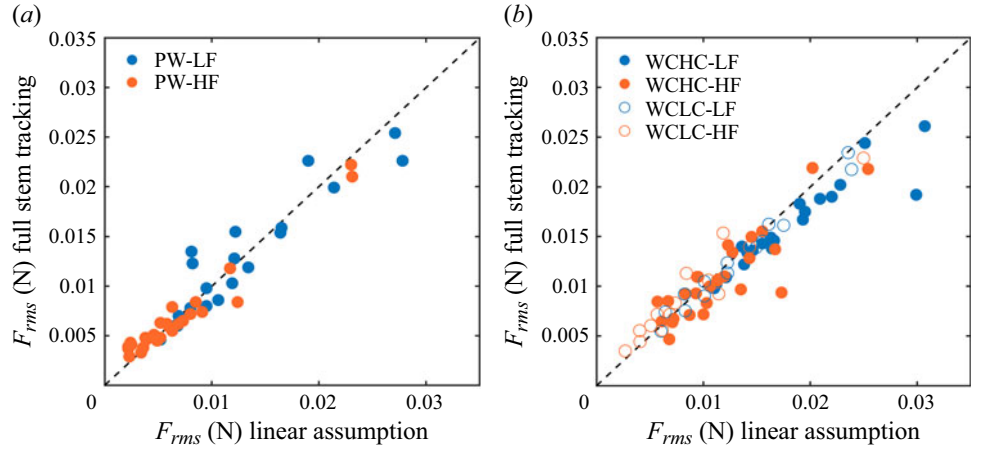


Figure 12. Comparison of force prediction on stems between along-stem velocities from linear assumptions and full-stem tracking under (*a*) PW conditions and (*b*) WCHC and WCLC conditions.

https://doi.org/10.1017/jfm.2025.10758 Published online by Cambridge University Press

force predictions. However, its applicability at higher CaL should be evaluated before broader applications.

It should be noted that neither approach can perfectly recover the true forces because the stems oscillate about their neutral configurations and the flow field varies spatially. Future work should incorporate the effects of spatiotemporal flow variation during stem motion.

Appendix C. Derivation of drag forces under orthogonal wave–current flows

The drag force is originally expressed as

$$F_D = \frac{1}{2}\rho C_D dl |u_r| u_r, \tag{C1}$$

where u_r is the relative velocity between the flow and the object (Denny *et al.* 1998). For rigid vegetation, u_r equals to flow velocity. Therefore, under pure waves and pure currents, u_r is equal to wave velocity (u_w) and current velocity (u_c), respectively. However, under orthogonal wave–current flows, u_r is equal to the total velocity (u_{wc}), which is the combination of wave and current velocities.

This study focuses on the water column from the bed to the stem height, where the depth-averaged velocity is close to the value of the mid-stem height. For simplicity, we assume u_w is uniform along the stem height and is approximated by its value at mid-stem height. Under the assumption of linear wave theory, the horizontal wave velocity is expressed as

$$u_w(\varphi, z) = a_w\omega\frac{\cosh(k(z+h))}{\sinh(kh)}\sin(\varphi) = \tilde{u}_w(z)\sin(\varphi), \tag{C2}$$

where the $\omega = 2\pi/T$ is the radian frequency, φ is the wave phase and k is the wavenumber. The amplitude of the horizontal wave orbital velocity at this height is given by $\tilde{u}_w = a_w\omega\cosh(k(l/2))/\sinh(kh)$. In the y-direction, a steady current velocity u_c is assumed. Then, u_{wc} is described by

$$u_{wc}(\varphi) = \sqrt{(\tilde{u}_w\sin(\varphi))^2 + u_c^2}. \tag{C3}$$

C.1. *Derivations of total drag*

Substituting the total velocity (C3) into (C1) yields the total drag force under orthogonal wave–current conditions,

$$F_D(\varphi) = \frac{1}{2}\rho C_D dl u_{wc}^2(\varphi) = \frac{1}{2}\rho C_D dl\left(\tilde{u}_w^2\sin^2\varphi + u_c^2\right). \tag{C4}$$

The total drag force force, which is in the same direction with $u_{wc}(\varphi)$, can be decomposed in the x- and y-directions. The decomposed drag, $\boldsymbol{F}_D(\varphi)$, at each direction can be expressed as

$$\boldsymbol{F}_D(\varphi) = \frac{1}{2}\rho C_D dl\sqrt{u_c^2 + \tilde{u}_w^2\sin^2\varphi}\begin{bmatrix} u_w\sin\varphi \\ u_c \end{bmatrix}, \tag{C5}$$

where the underline denotes a vector. Let $\beta = u_c/\tilde{u}_w$ be the current-to-wave velocity ratio and substitute into (C5), then $\boldsymbol{F}_D(\varphi)$ can be expressed as

$$\boldsymbol{F}_D(\varphi) = \frac{1}{2}\rho C_D dl\tilde{u}_w^2\sqrt{\beta^2 + \sin^2\varphi}\begin{bmatrix} \sin\varphi \\ \beta \end{bmatrix}. \tag{C6}$$

https://doi.org/10.1017/jfm.2025.10758 Published online by Cambridge University Press

C.2. *Derivations of time-averaged drag*

The time-averaged magnitude of the total drag force is expressed as

$$F_{D_{mean}} = \frac{1}{2\pi}\int_0^{2\pi} F_D(\varphi)\,\mathrm{d}\varphi = \frac{1}{2}\rho C_D dl\left(\frac{1}{2}\tilde{u}_w^2 + u_c^2\right). \tag{C7}$$

The decomposed components of the time-averaged total drag (C7) in the x- and y-directions can be obtained by integrating (C6) over one wave period from 0 to 2π, and dividing by 2π, yielding the following expressions:

$$\boldsymbol{F}_{D_{mean}} = \frac{1}{2}\rho C_D dl\tilde{u}_w^2\begin{bmatrix}\dfrac{\beta + (\beta^2+1)\arctan\dfrac{1}{\beta}}{\pi}\\ \beta^2 E\left(x\left|-\dfrac{1}{\beta^2}\right.\right)\Big|_0^{2\pi}\end{bmatrix}, \tag{C8}$$

where $E(x\,|\,-(1/\beta^2))$ denotes the elliptic integral of the second kind, which can be calculated using (C9). The elliptic integral arises naturally from the integration of $(\beta^2 + \sin^2\varphi)^{1/2}$ over a wave cycle for which no elementary solution exists. However, the elliptic integral of the second kind can be calculated numerically using the MATLAB function *ellipticE* (available in the *Symbolic Math Toolbox*).

$$E\left(x\,|\,-\frac{1}{\beta^2}\right) = \int_0^x \sqrt{1+\frac{\sin^2\varphi}{\beta^2}}\,\mathrm{d}\varphi. \tag{C9}$$

C.3. *Derivation of r.m.s. drag and maximum drag*

The r.m.s. magnitude of drag force that decomposed in the x- and y-direction can be expressed as

$$\boldsymbol{F}_{D_{rms}} = \sqrt{\frac{1}{2\pi}\int_0^{2\pi}\left(\boldsymbol{F}_D^2(\varphi)\right)\,\mathrm{d}\varphi} = \frac{1}{2}\rho C_D dl\tilde{u}_w^2\begin{bmatrix}\sqrt{\dfrac{4\beta^2+3}{8}}\\ \beta\sqrt{\beta^2+\dfrac{1}{2}}\end{bmatrix}, \tag{C10}$$

where boldface denotes a vector form and $\boldsymbol{F}_D(\varphi)$ is the decomposed drag force (C6).

The maximum drag corresponds to maximum $\tilde{u}_w \sin\varphi$ and can be expressed as

$$\boldsymbol{F}_{Dmax} = \frac{1}{2}\rho C_D dl\tilde{u}_w^2\sqrt{\beta^2+1}\begin{bmatrix}1\\ \beta\end{bmatrix}. \tag{C11}$$

References

Alben, S., Shelley, M. & Zhang, J. 2002 Drag reduction through self-similar bending of a flexible body. *Nature* **420** (6915), 479–481.

Almar, R., Larnier, S., Castelle, B., Scott, T. & Floc'h, F. 2016 On the use of the radon transform to estimate longshore currents from video imagery. *Coast. Engng* **114**, 301–308.

Augustin, L.N., Irish, J.L. & Lynett, P. 2009 Laboratory and numerical studies of wave damping by emergent and near-emergent wetland vegetation. *Coast. Engng* **56** (3), 332–340.

Barbier, E.B., Hacker, S.D., Kennedy, C., Koch, E.W., Stier, A.C. & Silliman, B.R. 2011 The value of estuarine and coastal ecosystem services. *Ecol. Monogr.* **81** (2), 169–193.

Barko, J.W. & James, W.F. 1998 Effects of submerged aquatic macrophytes on nutrient dynamics, sedimentation, and resuspension. In *The Structuring Role of Submerged Macrophytes in Lakes*, pp. 197–214. Springer.

https://doi.org/10.1017/jfm.2025.10758 Published online by Cambridge University Press

BETH SCHAEFER, R. & NEPF, H. 2022 Wave damping by seagrass meadows in combined wave-current conditions. *Limnol. Oceanogr.* **67** (7), 1554–1565.
BRADLEY, K. & HOUSER, C. 2009 Relative velocity of seagrass blades: implications for wave attenuation in low-energy environments. *J. Geophys. Res.: Earth Surf.* **114** (F1). https://doi.org/10.1029/2007JF000951
BURNETTE, C. & DALLY, W.R. 2017 The longshore transport enigma and analysis of a 10-year record of wind-driven nearshore currents. *J. Coast. Res.* **34** (1), 26–41.
COSTANZA, R., *et al.* 1997 The value of the world's ecosystem services and natural capital. *Nature* **387** (6630), 253–260
DENNY, M., GAYLORD, B., HELMUTH, B. & DANIEL, T. 1998 The menace of momentum: dynamic forces on flexible organisms. *Limnol. Oceanogr.* **43** (5), 955–968.
FOURQUREAN, J.W., *et al.* 2012 Seagrass ecosystems as a globally significant carbon stock. *Nat. Geosci.* **5** (7), 505–509.
GALVIN, C.J. 1967 Longshore current velocity: a review of theory and data. *Rev. Geophys.* **5** (3), 287–304.
GODA, Y. & SUZUKI, Y. 1976 Estimation of incident and reflected waves in random wave experiments. In *Coastal Engineering 1976*, pp. 828–845. https://doi.org/10.1061/9780872620834.048
GREINER, J.T., MCGLATHERY, K.J., GUNNELL, J. & MCKEE, B.A. 2013 Seagrass restoration enhances 'Blue carbon' sequestration in coastal waters. *PLOS ONE* **8** (8), e72469.
HOUSER, C., TRIMBLE, S. & MORALES, B. 2015 Influence of blade flexibility on the drag coefficient of aquatic vegetation. *Estuar. Coast.* **38** (2), 569–577.
INFANTES, E., ORFILA, A., SIMARRO, G., TERRADOS, J., LUHAR, M. & NEPF, H. 2012 Effect of a seagrass (Posidonia oceanica) meadow on wave propagation. *Mar. Ecol. Prog. Ser.* **456**, 63–72.
JACOBSEN, N.G., BAKKER, W., UIJTTEWAAL, W.S.J. & UITTENBOGAARD, R. 2019 Experimental investigation of the wave-induced motion of and force distribution along a flexible stem. *J. Fluid Mech.* **880**, 1036–1069.
KEULEGAN, G.H. & CARPENTER, L.H. 1958 Forces on cylinders and plates in an oscillating fluid. *J. Res. Natl Bur. Stand.* **60** (5), 423.
KOCH, E.W., *et al.* 2009 Non-linearity in ecosystem services: temporal and spatial variability in coastal protection. *Front. Ecol. Environ.* **7** (1), 29–37.
LECLERCQ, T. & DE LANGRE, E. 2018 Reconfiguration of elastic blades in oscillatory flow. *J. Fluid Mech.* **838**, 606–630.
LEE, W.K., TAY, S.H.X., OOI, S.K. & FRIESS, D.A. 2021 Potential short wave attenuation function of disturbed mangroves. *Estuar. Coast. Shelf Sci.* **248**, 106747.
LEI, J. & NEPF, H. 2016 Impact of current speed on mass flux to a model flexible seagrass blade. *J. Geophys. Res.: Oceans* **121** (7), 4763–4776.
LEI, J. & NEPF, H. 2019*a* Blade dynamics in combined waves and current. *J. Fluids Struct.* **87**, 137–149.
LEI, J. & NEPF, H. 2019*b* Wave damping by flexible vegetation: connecting individual blade dynamics to the meadow scale. *Coast. Engng* **147**, 138–148.
LEI, J. & NEPF, H. 2021 Evolution of flow velocity from the leading edge of 2-D and 3-D submerged canopies. *J. Fluid Mech.* **916**, A36.
LI, P., SHI, B., LI, Y., WANG, S., LV, X., WANG, Y.P. & TIAN, Q. 2020 Characterization of longshore currents in southern East China Sea during summer and autumn. *Acta Oceanol. Sin.* **39**, 1–11.
LIM, K.Y. & MADSEN, O.S. 2016 An experimental study on near-orthogonal wave–current interaction over smooth and uniform fixed roughness beds. *Coast. Engng* **116**, 258–274.
LOSADA, I.J., MAZA, M. & LARA, J.L. 2016 A new formulation for vegetation-induced damping under combined waves and currents. *Coast. Engng* **107**, 1–13.
LUHAR, M., INFANTES, E. & NEPF, H. 2017 Seagrass blade motion under waves and its impact on wave decay. *J. Geophys. Res.: Oceans* **122** (5), 3736–3752.
LUHAR, M. & NEPF, H.M. 2016 Wave-induced dynamics of flexible blades. *J. Fluids Struct.* **61**, 20–41.
LUHAR, M. & NEPF, H.M. 2011 Flow-induced reconfiguration of buoyant and flexible aquatic vegetation. *Limnol. Oceanogr.* **56** (6), 2003–2017.
LUHAR, M. & NEPF, H.M. 2013 From the blade scale to the reach scale: a characterization of aquatic vegetative drag. *Adv. Water Resour.* **51**, 305–316.
MAZA, M., LARA, J.L. & LOSADA, I.J. 2016 Solitary wave attenuation by vegetation patches. *Adv. Water Resour.* **98**, 159–172.
MENDEZ, F.J. & LOSADA, I.J. 2004 An empirical model to estimate the propagation of random breaking and nonbreaking waves over vegetation fields. *Coast. Engng* **51** (2), 103–118.
MULLARNEY, J.C. & HENDERSON, S.M. 2010 Wave-forced motion of submerged single-stem vegetation. *J. Geophys. Res.: Oceans* **115** (C12). https://doi.org/10.1029/2010JC006448

https://doi.org/10.1017/jfm.2025.10758 Published online by Cambridge University Press

PAUL, M. & AMOS, C.L. 2011 Spatial and seasonal variation in wave attenuation over Zostera noltii. *J. Geophys. Rese.: Oceans* **116** (C8). https://doi.org/10.1029/2010JC006797

PETROLO, D., UNGARISH, M., CHIAPPONI, L. & LONGO, S. 2022 Experimental study on radial gravity currents flowing in a vegetated channel. *J. Fluid Mech.* **933**, A46.

DE LOS SANTOS, C.B., ONODA, Y., VERGARA, J.J., PÉREZ-LLORÉNS, J.L., BOUMA, T.J., LA NAFIE, Y.A., CAMBRIDGE, M.L. & BRUN, F.G. 2016 A comprehensive analysis of mechanical and morphological traits in temperate and tropical seagrass species. *Mar. Ecol. Prog. Ser.* **551**, 81–94.

SCHAEFER, R. & NEPF, H. 2024 Movement of and drag force on slender flat plates in an array exposed to combinations of unidirectional and oscillatory flow. *J. Fluids Struct.* **124**, 104044.

SHERMAN, D.J. 1988 Empirical evaluation of longshore-current models. *Geographical Rev.* **78** (2), 158–168.

STRATIGAKI, V., MANCA, E., PRINOS, P., LOSADA, I.J., LARA, J.L., SCLAVO, M., AMOS, C.L., CÁCERES, I., SÁNCHEZ-ARCILLA, A. Large-scale experiments on wave propagation over *Posidonia oceanica*. *J. Hydraul. Res.* **49** (sup1), 31–43.

SUN, H., YOU, Y. & LEI, J. 2024 Deflection and drag on flexible marine structures in steady currents and internal solitary waves. *Phys. Fluids* **36** (10), 106603.

VETTORI, D. & MARJORIBANKS, T.I. 2021 Temporal variability and within-plant heterogeneity in blade biomechanics regulate flow-seagrass interactions of Zostera marina. *Water Resour. Res.* **57** (3). https://doi.org/10.1029/2020WR027747

WAYCOTT, M., LONGSTAFF, B.J. & MELLORS, J. 2005 Seagrass population dynamics and water quality in the Great Barrier Reef region: a review and future research directions. *Mar. Pollut. Bull.* **51** (1–4), 343–350.

VAN WESENBEECK, B.K., WOLTERS, G., ANTOLÍNEZ, J.A.A., KALLOE, S.A., HOFLAND, B., DE BOER, W.P., ÇETE, C. & BOUMA, T.J. 2022 Wave attenuation through forests under extreme conditions. *Sci. Rep-UK* **12** (1), 1884.

WIBERG, P.L., TAUBE, S.R., FERGUSON, A.E., KREMER, M.R. & REIDENBACH, M.A. 2019 Wave attenuation by Oyster Reefs in shallow coastal bays. *Estuar. Coast.* **42** (2), 331–347.

WOMERSLEY, H.B.S. 1984 *The Marine Benthic Flora of Southern Australia, Part 1*. Government Printer.

XIE, Y. & LEI, J. 2025 Laboratory investigation of solitary wave interactions with mangrove seedlings in hexagonal planters. *Coast. Engng* **203**, 104858.

XU, Z. & LEI, J. 2024*a* Experimental data for wave decay by submerged rigid vegetation under orthogonal wave-current conditions.

XU, Z. & LEI, J. 2024*b* Wave decay by submerged rigid vegetation under orthogonal wave-current conditions. *Geophys. Res. Lett.* **51** (23), e2024GL110408.

XU, Z. & LEI, J. 2025 Reconfiguration and hydrodynamic forces on flexible vegetation under orthogonal wave-current conditions.

ZELLER, R.B., WEITZMAN, J.S., ABBETT, M.E., ZARAMA, F.J., FRINGER, O.B. & KOSEFF, J.R. 2014 Improved parameterization of seagrass blade dynamics and wave attenuation based on numerical and laboratory experiments. *Limnol. Oceanogr.* **59** (1), 251–266.

ZHANG, R., CHEN, Y., LEI, J., ZHOU, X., YAO, P. & STIVE, M.J.F. 2023 Experimental investigation of wave attenuation by mangrove forests with submerged canopies. *Coast. Engng* **186**, 104403.

ZHANG, X., CHUA, V.P. & CHEONG, H.-F. 2015 Geometrical and material properties of Sonneratia alba mangrove roots. *Trees* **29** (1), 285–297.

ZHU, L., CHEN, Q., DING, Y., JAFARI, N., WANG, H. & JOHNSON, B.D. 2023 Towards a unified drag coefficient formula for quantifying wave energy reduction by salt marshes. *Coast. Engng* **180**, 104256.

ZHU, L., ZOU, Q.-P., HUGUENARD, K. & FREDRIKSSON, D.W. 2020 Mechanisms for the asymmetric motion of submerged aquatic vegetation in waves: a consistent-mass cable model. *J. Geophys. Res.: Oceans* **125** (2), e2019JC015517.

https://doi.org/10.1017/jfm.2025.10758 Published online by Cambridge University Press